



1 **Light absorption properties of aerosols over Southern** 2 **West Africa**

3

4 Cyrielle Denjean¹, Thierry Bourrienne¹, Frederic Burnet¹, Marc Mallet¹, Nicolas
5 Maury¹, Aurélie Colomb², Pamela Dominutti^{2,*}, Joel Brito^{2,**}, Régis Dupuy²,
6 Karine Sellegri², Alfons Schwarzenboeck², Cyrille Flamant³, Peter Knippertz⁴

7

8 ¹CNRM, Université de Toulouse, Météo-France, CNRS, Toulouse, France

9 ²LaMP, Université de Clermont Auvergne, Clermont-Ferrand, France

10 ³LATMOS/IPSL, Sorbonne Université, UVSQ, CNRS, Paris, France

11 ⁴Institute of Meteorology and Climate Research, Karlsruhe Institute of Technology,
12 Karlsruhe, Germany

13 * Now at Wolfson Atmospheric Chemistry Laboratories, Department of Chemistry,
14 University of York, YO10 5DD- York, UK

15 ** Now at: IMT Lille Douai, Université de Lille, SAGE, Lille, France

16

17 *Correspondence to : Cyrielle Denjean (cyrielle.denjean@meteo.fr)*

18

19 **Abstract.** Southern West Africa (SWA) is an African pollution hotspot but a relatively poorly
20 sampled region of the world. We present an overview of *in-situ* aerosol optical measurements
21 collected over SWA in June and July 2016 as part as the DACCIIWA (Dynamics-Aerosol-
22 Chemistry-Clouds Interactions in West Africa) airborne campaign. The aircraft sampled a wide
23 range of air masses, including anthropogenic pollution plumes emitted from the coastal cities,
24 long-range transported biomass burning plumes from Central and Southern Africa and dust plumes
25 from the Sahara and Sahel region, as well as mixtures of these plumes. The specific objective of
26 this work is to characterize the regional variability of the vertical distribution of aerosol particles
27 and their spectral optical properties (single scattering albedo: SSA, asymmetry parameter,
28 extinction mass efficiency, scattering Ångström exponent and absorption Ångström exponent:
29 AAE). First findings indicate that aerosol optical properties in the planetary boundary layer were
30 dominated by a widespread and persistent biomass burning loading from the Southern
31 Hemisphere. Despite a strong increase of aerosol number concentration in air masses downwind of
32 urban conglomerations, spectral SSA were comparable to the background and showed signatures of
33 the absorption characteristics of biomass burning aerosols. In the free troposphere, moderately to
34 strongly absorbing aerosol layers, dominated by either dust or biomass burning particles, occurred



35 occasionally. In aerosol layers dominated by mineral dust particles, SSA varied from 0.81 to 0.92 at
36 550 nm depending on the variable proportion of anthropogenic pollution particles externally mixed
37 with the dust. Biomass burning aerosol particles were significantly more light absorbing than those
38 previously measured in other areas (e.g. Amazonia, North America) with SSA ranging from 0.71 to
39 0.77 at 550 nm. The variability of SSA was mainly controlled by variations in aerosol composition
40 rather than in aerosol size distribution. Correspondingly, values of AAE ranged from 0.9 to 1.1,
41 suggesting that lens-coated black carbon particles were the dominant absorber in the visible range
42 for these biomass burning aerosols. Comparison with literature shows a consistent picture of
43 increasing absorption enhancement of biomass burning aerosol from emission to remote location
44 and underscores that the evolution of SSA occurred a long time after emission.
45 The results presented here build a fundamental basis of knowledge about the aerosol optical
46 properties observed over SWA during the monsoon season and can be used in climate modelling
47 studies and satellite retrievals. In particular and regarding the very high absorbing properties of
48 biomass burning aerosols over SWA, our findings suggest that considering the effect of internal
49 mixing on absorption properties of black carbon particles in climate models should help better
50 assessing the direct and semi-direct radiative effects of biomass burning particles.

51

52 **1. Introduction**

53 Atmospheric aerosols play a crucial role in the climate system by altering the radiation budget
54 through scattering and absorption of solar radiation and by modifying cloud properties and
55 lifetime. Yet considerable uncertainties remain about the contribution of both natural and
56 anthropogenic aerosol to the overall radiative effect (*Boucher et al., 2013*). Large uncertainties are
57 related to the complex and variable properties of aerosol particles that depend on the aerosol
58 source and nature as well as on spatial and temporal variations. During transport in the
59 atmosphere, aerosol particles may undergo physical and chemical aging processes altering the
60 composition and size distribution and henceforth the optical properties and radiative effects. The
61 capability of reproducing this variability in climate models represents a real challenge (*Myhre et*
62 *al., 2013; Stier et al., 2013; Mann et al., 2014*). Therefore, intensive experimental observations in
63 both aerosol source and remote areas are of paramount importance for constraining and evaluating
64 climate models.

65

66 Key parameters from a climate perspective are the aerosol vertical distribution and respective
67 spectral optical properties. Radiative transfer codes commonly incorporated in climate models and
68 in satellite data retrieval algorithms use single scattering albedo (SSA), extinction mass coefficient



69 (MEC) and asymmetry factor (g) as input parameters. These parameters depend on the aerosol size
70 distribution, the real and imaginary parts of the refractive index ($m-ik$), and the wavelength of
71 incident light, λ . The knowledge of the vertical distribution of these fundamental parameters is
72 crucial to accurately estimate the direct and semi-direct radiative effects of aerosols as well as the
73 vertical structure of atmospheric heating rates resulting from absorption by particles. Above
74 information is also required to retrieve aerosol properties (aerosol optical depth, size distribution)
75 from remote sensing data.

76
77 Southern West Africa (SWA) is one of the most climate-vulnerable region in the world, where the
78 surface temperature is expected to increase by $\sim 3^\circ\text{K}$ at the end of the century (2071-2100) in the
79 Coupled Model Intercomparison Project Phase 5 (CMIP5) (Roehrig *et al.*, 2013). It is
80 characterized by a fast-growing population, industrialization and urbanization (Lioussé *et al.*,
81 2014). This is particularly the case along the Guinea Coast where several already large cities are
82 experiencing rapid growth (Knippertz *et al.*, 2015a). Despite these dramatic changes, poor
83 regulation strategies of traffic, industrial and domestic emissions lead to a marked increase of
84 anthropogenic aerosol loading from multiple sources including road traffic, industrial activities,
85 waste burning, ship plumes, domestic fires, power plants, etc. Tangible evidence for regional
86 transport of anthropogenic pollutants associated with urban emissions has altered air pollution
87 from a local issue to a regional issue and beyond (Deetz *et al.*, 2018; Deroubaix *et al.* 2019). This
88 is particularly the case during summer when land-sea breeze systems can develop and promote the
89 transport of pollutants inland, away from the urbanized coastal strip of SWA (Flamant *et al.*,
90 2018a). In addition to this anthropogenic regional pollution, SWA is impacted by a significant
91 import of aerosols from remote sources. Biomass burning mainly from vegetation fires in Central
92 Africa are advected to SWA in the marine boundary layer and aloft (Mari *et al.*, 2008; Menut *et al.*
93 2018; Haslett *et al.*, 2019). The nearby Sahara desert and the Sahel are large sources of natural
94 wind-blown mineral dust aerosol throughout the year with a peak in springtime (Marticorena and
95 Bergametti, 1996). Biomass burning, dust and anthropogenic pollution aerosols can be mixed
96 along their transport pathways (Flamant *et al.*, 2018a; Deroubaix *et al.* 2019), resulting in
97 complex interactions between physical and chemical processes and even meteorological
98 feedbacks.

99
100 In West Africa, most of the aerosol–radiation interaction studies focused on optical properties of
101 dust and biomass burning aerosols in remote regions far from major sources of anthropogenic
102 pollution aerosol. They include ground-based and airborne field campaigns such as DABEX (Dust



103 and Biomass Experiment, *Haywood et al., 2008*), AMMA (Analysis Multidisciplinary of African
104 Monsoon, *Lebel et al., 2010*), DODO (Dust Outflow and Deposition to the Ocean, *McConnell et*
105 *al., 2008*), SAMUM-1 and SAMUM-2 (Saharan Mineral Dust Experiment, *Heintzenberg, 2009*;
106 *Ansmann et al., 2011*) and AER-D (AERosol Properties – Dust, *Ryder et al. 2018*). These projects
107 concluded that the influence of both mineral dust and biomass burning aerosols on the radiation
108 budget is significant over West Africa, implying that meteorological forecast and regional/global
109 climate models should include their different radiative effects for accurate forecasts and climate
110 simulations. Over the Sahel region, *Solmon et al. (2008)* have highlighted the high sensitivity of
111 mineral dust optical properties to precipitation changes at a climatic scale. However, the optical
112 properties of aerosols particles in the complex chemical environment of SWA are barely studied.
113 This is partly due to the historically low level of industrial developments of the region. Motivated
114 by the quickly growing cities along the Guinea Coast, the study of transport, mixing, and feedback
115 processes of aerosol particles is therefore very important for better quantification of aerosol
116 radiative impact at the regional scale and improvement of climate and numerical weather
117 prediction models.

118

119 In this context, the DACCIWA (Dynamics-Aerosol-Chemistry-Clouds Interactions in West Africa,
120 *Knippertz et al., 2015b*) campaign, designed to characterize both natural and anthropogenic
121 emissions over SWA, provides important and unique observations of aerosols in a region much
122 more affected by anthropogenic emissions than previously thought. A comprehensive field
123 campaign took place in June–July 2016 including extensive ground-based (*Kalthoff et al., 2018*)
124 and airborne measurements (*Flamant et al., 2018b*). In this study, we present an overview of *in-*
125 *situ* airborne measurements of the vertical distribution of aerosol particles and their spectral optical
126 properties acquired with the ATR-42 French research aircraft over the Guinea Coast.

127

128 Section 2 presents the flight patterns, instrumentation and data analysis. Section 3 provides an
129 overview of the aerosol microphysical and optical properties. The impact of aging and mixing
130 processes on aerosol optical properties is discussed in section 4 before conclusions are presented in
131 section 5.

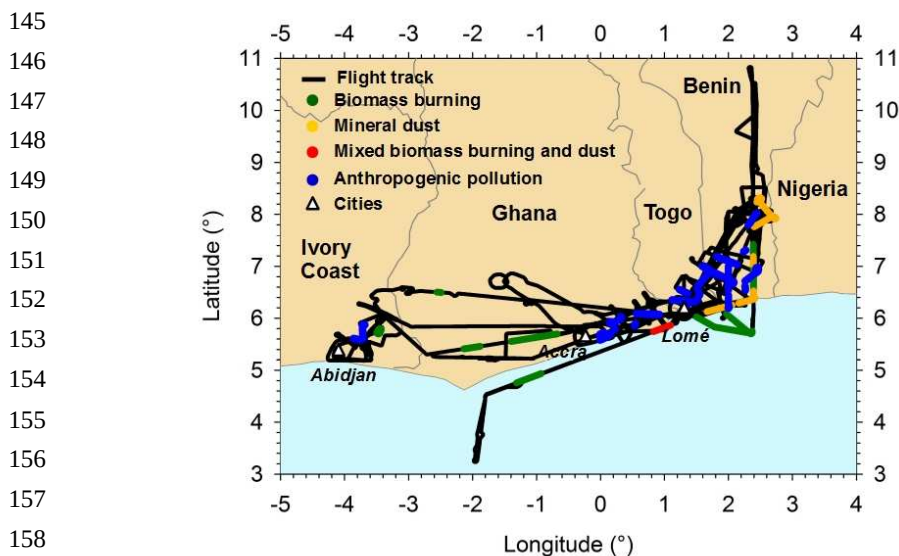
132



133 2. Methodology

134 2.1. ATR-42 measurements overview

135 This analysis focuses on flight missions conducted by the ATR-42 aircraft of SAFIRE (Service des
136 Avions Français Instrumentés pour la Recherche en Environnement - the French aircraft service
137 for environmental research) over the Gulf of Guinea and inland. A full description of flight
138 patterns during DACCIWA is given in *Flamant et al. (2018b)*. Here we present results from 15
139 flights focused on the characterization of anthropogenic pollution, dust and biomass burning
140 plumes. The flight tracks are shown in Figure 1 and a summary of flight information is provided in
141 Appendix 1. The sampling strategy generally consisted of two parts: first, vertical soundings were
142 performed from 60 m up to 8 km above mean sea level (amsl) to observe and identify interesting
143 aerosol layers. Subsequently, the identified aerosol layers were probed with the *in-situ* instruments
144 by straight levelled runs (SLR) at fixed flight altitudes.



157
158
159
160 **Figure 1. Tracks of the 15 flights analyzed in this study. The colors indicate aircraft flight**
161 **levels sampling layers dominated by biomass burning (green), mineral dust (orange), mixed**
162 **dust-biomass burning (red) and anthropogenic pollution particles (blue).**
163

164 The ATR-42 aircraft was equipped with a wide variety of instrumentation performing gas and
165 aerosol measurements. The measured meteorological parameters include temperature, dew point
166 temperature, pressure, turbulence, relative humidity, as well as wind speed and direction. Gas
167 phase species were sampled through a rear facing ¼ inch Teflon tube. Carbon monoxide (CO) was



168 measured using ultra-violet and infrared analysers (PICARRO). The nitric oxide (NO) and
169 nitrogen dioxide (NO₂) measurements were performed using an ozone chemiluminescence
170 instrument (Thermo Environmental Instrument TEi42C with a Blue Light Converter for the NO₂
171 conversion). On-board aerosol instruments sampled ambient air via stainless steel tubing through
172 the Community Aerosol Inlet (CAI). This is an isokinetic and isoaxial inlet with a 50 % sampling
173 efficiency for particles with a diameter of 5 μm (*Denjean et al., 2016*).

174

175 The total number concentration of particles larger than 5 nm (*N_{tot}*) was measured by a
176 condensation particle counter (CPC model MARIE built by University of Mainz). The aerosol size
177 distribution was measured using an ultra-high sensitivity aerosol spectrometer (UHSAS, DMT), a
178 custom-built scanning mobility sizer spectrometer (SMPS) and an optical particle counter (OPC,
179 GRIMM model 1.109). Instrument calibration was performed with PSL nanospheres and oil
180 particles size-selected by a differential mobility analyser (DMA) for diameters from 90 nm to 20
181 μm. The SMPS data acquisition system failed after two-third of the campaign and could not be
182 repaired. We found the UHSAS to show false counts in the diameters below 100 nm. Therefore,
183 these channels were disregarded in the data analysis.

184

185 The particle extinction coefficient (σ_{ext}) at the wavelength of 530 nm was measured with a cavity
186 attenuated phase shift particle light extinction monitor (CAPS-PMex, Aerodyne Research). The
187 particle scattering coefficients (σ_{scat}) at 450, 525 and 700 nm were measured using a TSI 3-
188 wavelength nephelometer. The absorption coefficients (σ_{abs}) at 467, 520 and 660 nm were
189 measured by a Radiance Research Particle Soot Absorption Photometer (PSAP). The PSAP
190 measures changes of filter attenuation due to the collection of aerosol deposited on the filter, which
191 were corrected for the scattering artifacts according to the *Virkkula (2010)* method. Prior to the
192 campaign, the CAPS was evaluated against the combination of the nephelometer and the PSAP. An
193 instrument intercomparison was performed with purely scattering ammonium sulfate particles and
194 with strongly absorbing black carbon particles (BC). Both types of aerosol were generated by
195 nebulizing a solution of the respective substances and size-selected using a DMA. For instrument
196 intercomparison purposes, σ_{ext} from the combination of nephelometer and PSAP was adjusted to
197 that for 530 nm by using the scattering and absorption Ångstrom exponent (*SAE* and *AAE*,
198 respectively). The instrument evaluation showed an excellent accuracy of the CAPS measurements
199 by comparison to the nephelometer and PSAP combination.

200



201 **2.2. Ancillary products**

202 In order to determine the history of air masses prior aircraft sampling, backward trajectories and
203 satellite images were used. The trajectories were computed using the Hybrid Single Particle
204 Lagrangian Integrated Trajectory Model (HYSPLIT) and the National Centers for Environmental
205 Prediction (NCEP) Global Data Assimilation System (GDAS) data with 0.5° horizontal resolution
206 for sequences and times of interest. We compared the backward trajectory heights with information
207 of fire burning times (e.g. MODIS Burnt Area Product) and dust release periods (e.g. Meteosat
208 Second Generation (MSG) dust RGB composite images) to assess the aerosol source regions of the
209 investigated air masses. The air masses represented by the trajectory are assumed to obtain their
210 aerosol loading from source regions when the trajectory passes over regions with significant dust
211 activation and/or fire activity at an altitude close to the surface. Trajectory calculations with
212 slightly modified initial conditions with respect to the arrival time, location and altitude were
213 performed to check the reliability of the location of source regions. Uncertainties in this approach,
214 caused by unresolved vertical mixing processes, and by general uncertainties of the trajectory
215 calculations are estimated to be in the range of 15–20 % of the trajectory distance (*Stohl et al.*,
216 2002).

217

218 **2.3. Data analysis**

219 In the following, extensive aerosol parameters (concentrations, scattering, absorption and
220 extinction coefficients) are converted to standard temperature and pressure (STP) using $T = 273$ K
221 and $P = 1013.25$ hPa. The STP concentration data correspond to mixing ratios, which are
222 independent of ambient pressure and temperature during the measurement. In the analysis, the data
223 were averaged over sections of SLR with homogeneous aerosol conditions outside of clouds.

224

225 **2.3.1. Derivation of aerosol microphysical and optical properties**

226 Appendix 2 and Table 1 show the iterative procedure and the equations used to calculate the
227 aerosol microphysical and optical parameters as briefly explained below.

228

229 The particle number concentration in the coarse mode (N_{coarse}) was calculated by integrating the
230 OPC size distributions over the range 1 to 5 μm . The number concentration of particles in the fine
231 mode (N_{fine}) was obtained as the difference between total number concentration (N_{tot} particle
232 diameter range above 5 nm) measured by the CPC and N_{coarse} .

233



234 For optical calculations, the $3\lambda\text{-}\sigma_{abs}$ from the PSAP were adjusted at the 3 wavelengths measured
235 by the nephelometer using the *AAE* calculated from the 3λ measured σ_{abs} . Once σ_{scat} and σ_{abs}
236 obtained at the same wavelength, an optical closure study estimated the complex refractive index
237 based on optical and size data. Optical calculations were performed using Mie theory for spherical
238 particles by varying stepwise the real part of the complex refractive index (*m*) from 1.33 to 1.60
239 and the imaginary part of the complex refractive index (*k*) from 0.000 to 0.080. Given that the size
240 distribution measured by the UHSAS and the OPC depends on *n*, the optical-to-geometrical
241 diameter conversion was recalculated at each iteration based on the assumed *n*. The resulting
242 number size distributions from SMPS, UHSAS and OPC were parameterized by fitting four log-
243 normal distributions and used as input values in the optical calculations. *m* and *k* were fixed when
244 the best agreement between calculated values of σ_{scat} and σ_{abs} and measurements was found. Once
245 *n* and *k* were obtained at 3λ , we estimated the following optical parameters:

246 - *SAE* depends on the size of the particles. Generally, it is lower than 0 for aerosols dominated by
247 coarse particles, such as dust aerosols, but it is higher than 0 for fine particles, such as
248 anthropogenic pollution or biomass burning aerosol (Seinfeld and Pandis, 2006; Schuster et al.,
249 2006).

250 - *AAE* provides information about the chemical composition of atmospheric aerosols. BC absorbs
251 radiation across the whole solar spectrum with the same efficiency, thus it is characterized by *AAE*
252 values around 1. Conversely, mineral dust particles show strong light absorption in the blue to
253 ultraviolet spectrum leading to *AAE* values up to 3 (Kirchstetter et al., 2004; Petzold et al., 2009).

254 - *SSA* describes the relative importance of scattering and absorption for radiation. Thus, it indicates
255 the potential of aerosols for cooling or warming the lower troposphere.

256 - *g* describes the probability of radiation to be scattered in a given direction. Values of *g* can range
257 from -1 for entirely backscattered light to +1 for complete forward scattering light.

258 - *MEC* represents the total light extinction per unit mass concentration of aerosol. The estimates of
259 *MEC* assume mass densities of 2.65 g cm³ for dust aerosol, 1.35 g cm³ for biomass burning
260 aerosol, 1.7 g cm³ for anthropogenic aerosol and 1.49 g cm³ for background aerosol (Hess et al.,
261 1998; Haywood et al., 2003a).



262

Aerosol parameters	Symbol	λ (nm)	Method
Aerosol microphysical properties			
Total number concentration	N_{tot}	-	Measured by a CPC in the particle diameter range above 5 nm
Number concentration in the coarse mode	N_{coarse}	-	GRIMM size distributions integrated on the range 1 to 5 μm .
Number concentration in the fine mode	N_{fine}	-	Difference N_{tot} and N_{coarse} .
Number size distribution	$dN/d\log D_p$	-	$dN/d\log D_p = \sum_{i=1}^4 (N_{tot,i} \exp(-(\log D_p - \log D_{p,g,i})^2 / (2 \log \sigma_i)) / (\sqrt{2 \log \sigma_i}))$ with $N_{tot,i}$ the integrated number concentration, $D_{p,g,i}$ the geometric median diameter and σ_i geometric standard deviation for each mode i
Volume size distribution	$dV/d\log D_p$	-	$dV/d\log D_p = \sum_{i=1}^4 (N_{tot,i} D_p^3 \pi / 6 \exp(-(\log D_p - \log D_{p,g,i})^2 / (2 \log \sigma_i)) / (\sqrt{2 \log \sigma_i}))$
Aerosol optical properties			
Scattering coefficient	σ_{scat}	450, 550, 700	Measured by the nephelometer and corrected for truncator error
Absorption coefficient	σ_{abs}	467, 520, 660	Measured by the PSAP and corrected for filter based artefacts
Extinction coefficient	σ_{ext}	530	Measured by the CAPS
Scattering Ångström exponent	SAE	450 to 700	Calculated from the nephelometer measurements : $SAE = -\ln(\sigma_{scat}(450)/\sigma_{scat}(700)) / \ln(450/700)$
Absorption Ångström exponent	AAE	440 to 660	Calculated from the PSAP measurements : $AAE = -\ln(\sigma_{abs}(467)/\sigma_{abs}(660)) / \ln(467/660)$
Complex refractive index	n	450, 550, 660	Inversion closure study using Mie theory (Fig. A2) $n(\lambda) = m(\lambda) - ik(\lambda)$
Single scattering albedo	SSA	450, 550, 660	Inversion closure study using Mie theory (Fig. A2) $SSA(\lambda) = \sigma_{scat}(\lambda) / \sigma_{ext}(\lambda)$
Mass extinction efficiency	MEC	450, 550, 660	Inversion closure study using Mie theory (Fig. A2) $MEC(\lambda) = \sigma_{ext}(\lambda) / C_m$ with C_m the aerosol mass concentration
Asymmetry parameter	g	450, 550, 660	Inversion closure study using Mie theory (Fig. A2) $g(\lambda) = 1/2 \int_0^\pi \cos(\Theta) \sin(\Theta) P(\Theta, \lambda) d(\Theta)$ with $P(\Theta, \lambda)$ the scattering phase function and Θ the scattering angle.

263

Table 1. Aerosol microphysical and optical properties derived in this work

264



265 **2.3.2. Classification of aerosols plumes**

266 Data were screened in order to isolate plumes dominated by anthropogenic pollution from urban
267 emissions, biomass burning and mineral dust particles, resulting in a total number of 19, 12 and 8
268 genuine plume interceptions, respectively, across the 15 flights. Identification of the plumes was
269 based on a combination of CO and NO_x (sum of NO and NO₂) concentrations, as well as AAE and
270 SAE that have been shown to be good parameters for classifying aerosol types (Kirchstetter *et al.*,
271 2004; Petzold *et al.*, 2009). The classification was then compared with results from the back
272 trajectory analysis (Figure 2) and satellite images described in section 2.2. The guidelines for
273 classification are as follows:

274 - *Anthropogenic pollution*: SAE was beyond threshold 0, indicating a large number fraction of
275 small particles in urban plumes, and CO and NO_x concentrations 2 times higher than the
276 background concentrations. During the DACCIWA campaign background CO and NO_x values
277 were around 180 ppb and 0.28 ppb, respectively. The trajectories show large differences in the
278 flow patterns and source regions with urban plumes originating from the polluted cities of Lomé,
279 Accra and Abidjan. The aircraft sampling over land mostly followed the north-eastward direction
280 (Figure 2d).

281 - *Biomass burning*: The criteria are the same as for urban pollution plumes except that trajectories
282 track these plumes back to active fire hotspots as observed by MODIS and the ratio NO_x to CO
283 was set below 1. CO and NO_x are byproducts of combustion sources but CO is preserved longer
284 along the plume when compared with NO_x, which makes the ratio NO_x to CO a good indicator for
285 distinguishing fresh anthropogenic pollution plumes from biomass burning plumes transported
286 over long distances (Wang *et al.*, 2002; Silva *et al.*, 2017). During this time of the year, most of the
287 forest and grassland fires were located in Central and Southern Africa (Figure 2a).

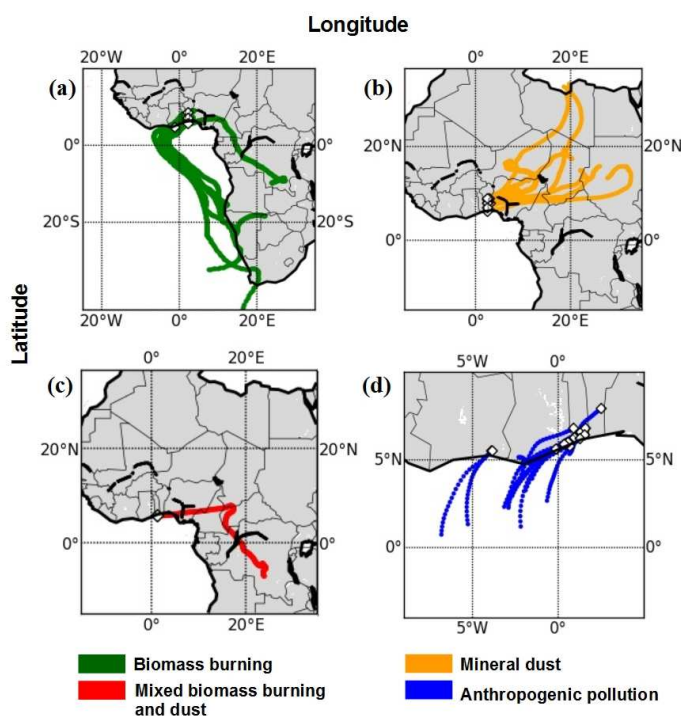
288 - *Mineral dust*: AAE higher than 1 indicates a large mass fraction of mineral dust and a SAE below
289 0 indicate a high effective particle diameter. The source region of the dust loaded air masses was
290 located in the Saharan desert and in the Sahel (Figure 2b).

291 - *Dust and biomass burning mixing*: Combining remote sensing observations and model
292 simulations, Flamant *et al.* (2018a) identified a biomass burning plume mixed with mineral dust.
293 This agrees well with the measured AAE of 1.2 and SAE of 0.3 observed in this layer. Menut *et al.*
294 (2018) have shown that one of the transport pathways of biomass burning aerosols from Central
295 Africa was associated with northward advection towards Chad and then westward displacement
296 linked to the African Easterly Jet. The plume originated from a broad active biomass burning area
297 including Gabon, the Republic of Congo and the Democratic Republic of Congo and passed over



298 areas with strong dust emissions further north within 1–3 days before being sampled by the aircraft
299 (Figure 2c).

300 - *Background*: We refer to background conditions as an atmospheric state in the boundary layer
301 without the detectable influence of local anthropogenic pollution sources. Most back trajectories
302 originated from the marine atmosphere and coastal areas south of the sampling area.



303 **Figure 2. Backward trajectories for the analyzed aerosol layers. Trajectories date**
304 **back 10 days for (a), 5 days for (b) and (c), and 1 day for (d).**

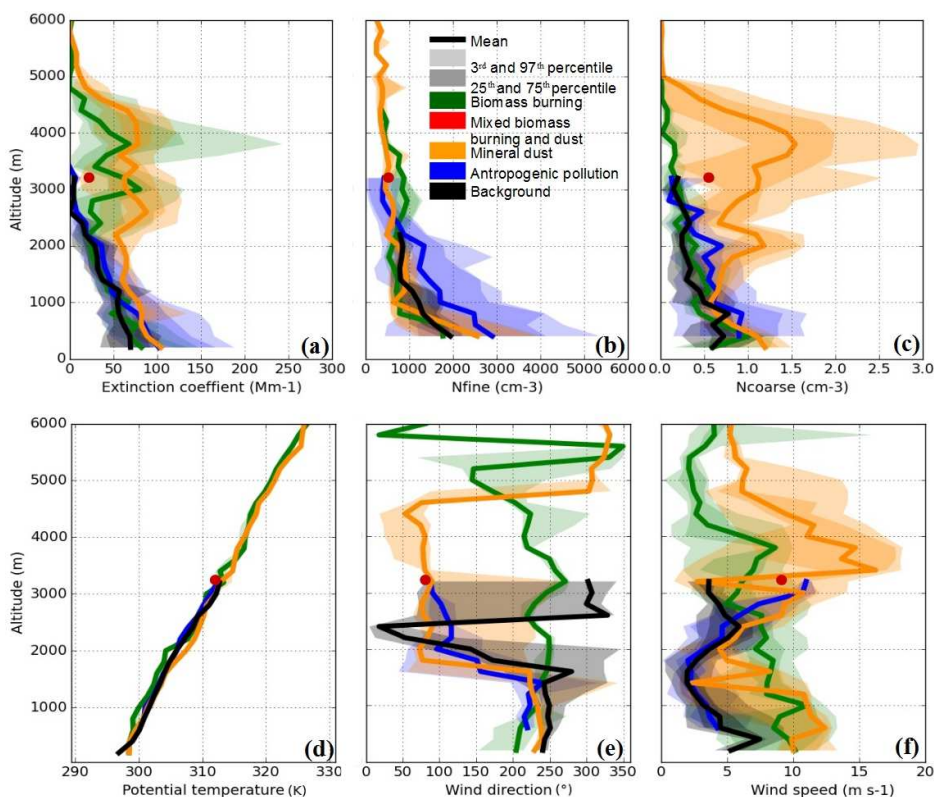
306 3. Results

307 3.1. Aerosol vertical distribution

308 Figure 3 shows a statistical analysis of N_{fine} , N_{coarse} and σ_{ext} derived from the *in-situ* measurements
309 of vertical profiles. The aerosol vertical structure is strongly related to the meteorological structure
310 of the atmosphere (see Knippertz *et al.*, 2017 for an overview of the DACCIIWA field campaign).
311 Therefore wind vector and potential temperature profiles acquired with the aircraft have been
312 added to Figure 3 as a function of the dominating aerosol composition, introduced in Figure 1. The



313 data from individual vertical profiles were merged into 200 m vertical bins from the surface to
314 km amsl. The profiles were calculated using only individual profiles obtained outside of clouds.
315



316 **Figure 3. Vertical layering of aerosols and meteorological variables for profiles for which**
317 **aerosols dominated by biomass burning (green), dust (orange), mixed dust-biomass burning**
318 **(red), anthropogenic pollution (blue) and background particles (black) were detected. The**
319 **panels show profiles of (a) the extinction coefficient at 530 nm, (b) the particle number**
320 **concentration in the range $0.005 < D_p < 1 \mu\text{m}$, (c) the particle number concentration in the**
321 **range $1 < D_p < 5 \mu\text{m}$, (d) potential temperature, (e) the wind direction and (f) the wind speed.**
322 **The colored areas represent the 3rd, 25th, 75th and 97th percentiles of the data. The mixed dust-**
323 **biomass burning plume is represented by a dot because it is derived from measurements**
324 **during a SLR.**
325

326 The observed wind profiles highlight the presence of several distinct layers in the lower
327 troposphere. For cases related to dust, urban pollution and background condition, we clearly
328 observe the monsoon layer up to 1.5 km amsl which is characterized by weak to moderate wind
329 speeds (2 to 10 m s^{-1} , the later corresponding to dust cases) and a flow from the southwest (220-



330 250°). In all three air mass regimes, the monsoon layer is topped by a 500 to 700 m deep layer
331 characterised by a sharp wind direction change (from south-westerly to easterly). Weak wind
332 speeds (less than 5 m s⁻¹) are observed in urban pollution and background conditions, while higher
333 wind speeds are observed in the dust cases. Above 2.5 km amsl, the wind speed increases in the
334 urban pollution and dust cases and the wind remains easterly, indicating the presence of the
335 African easterly jet with its core typically farther north over the Sahel. The maximum easterlies
336 are observed in the dust cases slightly below 3.5 km amsl (> 15 m s⁻¹). For the background cases,
337 the wind above the shear layer shifts to north-westerly and remains weak (~i.e. 5 m s⁻¹). Overall,
338 the wind profile associated with the biomass burning cases is quite different from the other three
339 cases, with a flow essentially from the south-southwest below 5 km amsl and higher wind speeds
340 in the lower 2 km amsl than above, and a secondary maximum of 7 m s⁻¹ at 4 km amsl.

341
342 The vertical distribution of aerosol particles was very inhomogeneous, both across separate
343 research flights and between individual plumes encountered during different periods of the same
344 flight. Measurements of aerosols within this analysis cover a broad geographic region, as shown in
345 Figure 1, which may explain some of the variability. SWA is subject to numerous anthropogenic
346 emission sources (e.g. road traffic, heavy industries, open agriculture fires, etc.) coupled to
347 biogenic emissions from the ocean and forests. These resulting large emissions are reflected in the
348 high variability of σ_{ext} , N_{fine} and N_{coarse} in the lower troposphere over SWA. Below 2.5 km amsl, σ_{ext}
349 showed a large heterogeneity with values ranging from 35 to 188 Mm⁻¹ between the 3rd and 97th
350 percentile and a median value of 55 Mm⁻¹. The variability of σ_{ext} values was slightly enhanced near
351 the surface and was correlated to N_{fine} and N_{coarse} which ranged from 443 to 5250 cm⁻³ and from
352 0.15 to 1.6 cm⁻³, respectively. Maximum surface σ_{ext} was recorded in the anthropogenic pollution
353 plume of Accra where high N_{fine} was sampled. The aerosol vertical profile is strongly modified
354 during biomass burning and dust events. The dust plume extends from 2 to 5 km amsl, and is
355 associated with transport from the dust sources in Chad and Sudan (see Figure 2) with the midlevel
356 easterly flow. The biomass burning plume is associated with transport from the southwest in a
357 layer of enhanced wind speed just below 4 km amsl as discussed above. Both layers showed
358 enhanced σ_{ext} with median values of 68 Mm⁻¹ ($p_{03} = 12 \text{ Mm}^{-1}$; $p_{97} = 243 \text{ Mm}^{-1}$) in biomass burning
359 plumes and 78 Mm⁻¹ ($p_{03} = 45 \text{ Mm}^{-1}$; $p_{97} = 109 \text{ Mm}^{-1}$) in dust plumes. As expected, the extinction
360 profile was strongly correlated to N_{fine} for biomass burning layers and N_{coarse} for dust layers.

361
362 A prominent feature in the vertical profiles is the presence of fine particles up to 2.5 km amsl
363 outside of biomass burning or dust events. σ_{ext} , N_{fine} and N_{coarse} continuously decrease with altitude,

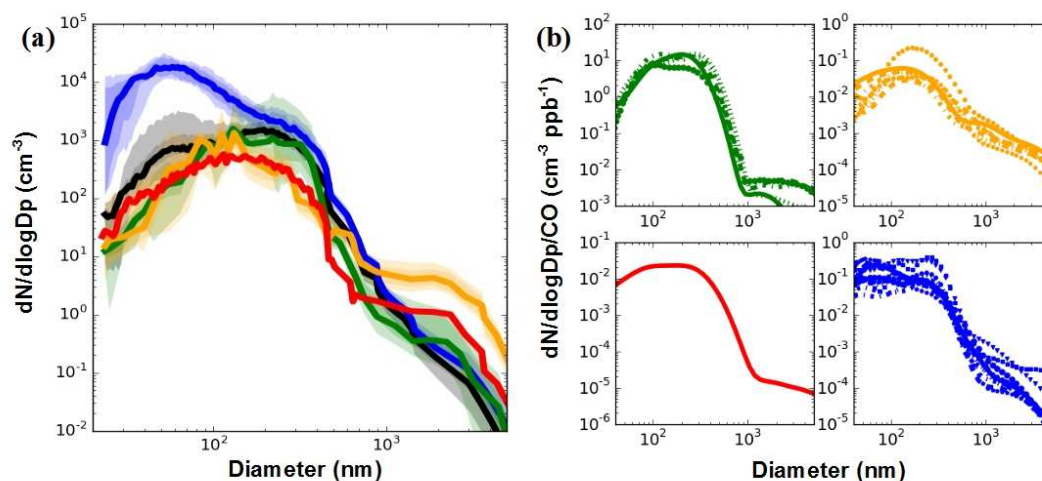


364 most likely due to vertical mixing of local emissions from the surface to higher levels. Therefore,
365 the regional transport of locally emitted aerosols was not limited to the surface but occurred also at
366 higher altitude. Recently, numerical tracer experiments performed for the DACCIWA airborne
367 campaign period have demonstrated that a combination of land–sea surface temperature gradients,
368 orography-forced circulation and the diurnal cycle of the wind along the coastline favor the
369 vertical dispersion of pollutants above the boundary layer during daytime (*Deroubaix et al., 2019*;
370 *Flamant et al., 2018a*). Because of these complex atmospheric dynamics, aerosol layers transiting
371 over the Gulf of Guinea in the free troposphere could be contaminated by background or urban
372 pollution aerosols from the major coastal cities.

373

374 3.2. Aerosol size distribution

375 Figure 4a shows the range of variability of the number and volume size distributions measured
376 during DACCIWA. These are extracted from the SLRs identified in Fig.1. Figure 4b shows the
377 same composite distribution normalized by CO concentration in order to account for differences in
378 the amount of emissions from combustion sources.



379 **Figure 4.** (a) Statistical analysis of number size distributions with colored areas representing
380 the 3th, 25th, 75th and 97th percentiles of the data and (b) number size distributions normalized
381 to CO for plumes dominated by biomass burning (green), dust (orange), mixed dust-biomass
382 burning (red), anthropogenic pollution (blue) and background particles (black).
383

384 Considerable variability in the number concentration of the size distributions, up to approximately
385 2 orders of magnitude, was observed for a large fraction of the measured size range. The size



386 distributions varied both for different aerosol types and for a given aerosol class. This reflects the
387 relative wide range of different conditions that were observed over the region, both in terms of
388 sources, aerosol loading, and lifetimes of the plumes.

389

390 In particular for ultrafine particles with diameters below 100 nm, large differences are observed,
391 with an increase as large as a factor of 50 in urban plumes, which reflects concentration increase
392 from freshly formed particles. Interestingly elevated number concentrations of these small-
393 diameter particles were also observed in some dust layers. Comparing the particle size distribution
394 of the different dust plumes sampled during the field campaign, a variation as large as a factor of
395 20 in the number concentration of ultrafine particles is found. Their contribution decreased with
396 height as reflected by higher small particle number recorded in dust plumes below 2.5 km amsl
397 (Figure 3b and 4b). As the composite urban size distributions showed a relatively similar ultrafine
398 mode centered at 50 nm, dust layers have most likely significant contributions from anthropogenic
399 pollution aerosol freshly emitted in SWA. The ultrafine mode was not observed in biomass
400 burning size distributions, even though dust and biomass burning plumes were sampled in the
401 same altitude range. We interpret this observation with dust plumes transported below 2.5 km amsl
402 that were sampled over the region of Savè (8°01'N, 2°29'E; Benin) near the identified urban air
403 mass transported northeastwards from Lomé and/or Accra and which may have collected
404 significant fresh pollution on their way, whereas biomass burning plumes collected at the same
405 altitude and sampled over Ivory Coast south of the Abidjan pollution plumes may not have been
406 affected by significant direct pollution (Figure 1).

407

408 The accumulation mode was dominated by two modes centered at $D_{p,g} \sim 100$ and 230 nm
409 depending on the aerosol plume. The particle size distributions for biomass burning plumes were
410 generally dominated by an accumulation mode centered at $D_{p,g} \sim 230$ nm. Despite the relative wide
411 range of sources and lifetimes of the biomass burning plumes sampled throughout the campaign
412 (Figure 2), the $D_{p,g}$ in the accumulation mode showed little variation ($D_{p,g}$ from 210 to 270 nm)
413 between the plumes. Similarly, previous field studies found accumulation mode mean diameters
414 from 175 to 300 nm for aged biomass burning plumes, regardless of their age, transport time and
415 source location (Capes *et al.*, 2008; Janhäll *et al.*, 2010; Weinzierl *et al.*, 2011; Sakamoto *et al.*,
416 2015; Carrico *et al.* 2016). The coagulation rate can be very high in biomass burning plumes and
417 can shape the size distribution over a few hours (Sakamoto *et al.*, 2016). It is worth noting that in
418 the biomass burning and dust size distributions there is a persistent particle accumulation mode
419 centered at ~ 100 nm that exceeds the amount of larger particles in some layers. This small mode is



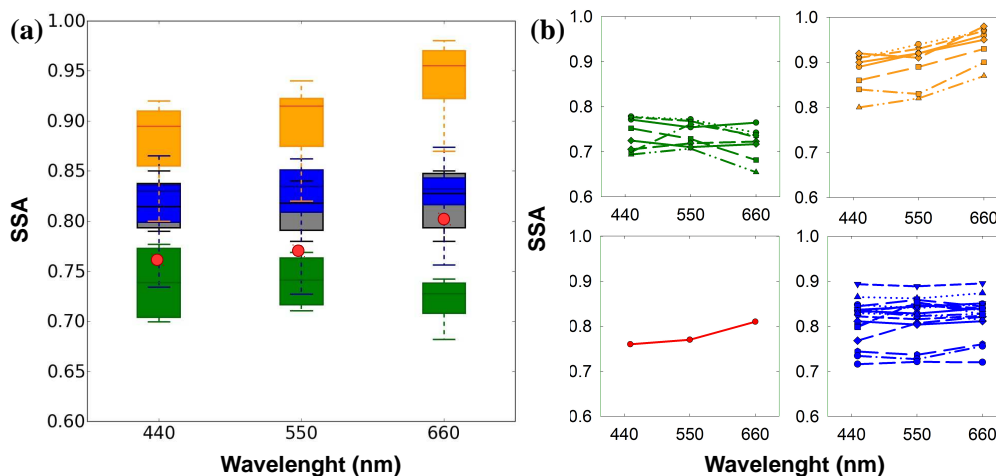
420 unlikely to be related to long-range transport of biomass burning and Saharan dust emissions, as it
421 would be expected that particles in this size range would grow to larger particles through
422 coagulation relatively quickly. As similar concentrated accumulation modes of particles have been
423 observed in background plumes, it suggests the entrainment of background air from the boundary
424 layer in dust and biomass burning plumes. This is supported by remote sensing observations on 2
425 and 5 July 2016 (Flamant *et al.*, 2018a; Deroubaix *et al.*, 2019).

426
427 The number concentration of large super-micron particles was strongly enhanced in the mineral
428 dust layers. The peak number concentration displayed a broad shape at $D_{p,g} \sim 1.8 \mu\text{m}$, which is
429 comparable to literature values of other long-range transported dust aerosols (Weinzierl *et al.*,
430 2011; Ryder *et al.*, 2013; Denjean *et al.*, 2016; Liu *et al.*, 2018). The relatively homogeneous $D_{p,g}$
431 in the coarse mode of dust ($D_{p,g}$ from 1.7 to 2.0 μm) suggests low internal mixing with other
432 atmospheric species. Besides, the volume size distribution in urban plumes showed significant
433 presence ($\sim 65\%$ of the total aerosol volume) of large particles with diameters of $\sim 1.5 - 2 \mu\text{m}$,
434 which were also observed in background conditions. This coarse mode has most likely significant
435 contributions from sea salt particles, as plumes arriving from the cities were transported at low
436 altitude over the ocean (Fig. 3).

437

438 3.3. Aerosol optical properties

439 SSA is one of the most relevant intensive optical properties because it describes the relative
440 strength of the aerosol scattering and absorption capacity and is a key input parameter in climate
441 models (Solmon *et al.*, 2008). Figure 5 shows the spectral SSA for the different SLRs considered in
442 this study.



443

444 **Figure 5. (a) Statistical analysis of single scattering albedo at 450, 550 and 660 nm for**
445 **plumes dominated by biomass burning (green), dust (orange), mixed dust-biomass burning**
446 **(red), anthropogenic pollution (blue) and background particles (black). The boxes enclose the**
447 **25th and 75th percentiles, the whiskers represent the 5th and 95th percentiles and the**
448 **horizontal bar represents the median. (b) Spectral SSA for the different individual plumes**
449 **considered in this study. The mixed dust-biomass burning plume is represented by a dot**
450 **because it is derived from measurements during only one SLR.**
451

452 The highest absorption (lowest SSA) at all three wavelengths was observed for biomass burning
453 aerosols. SSA values ranged from 0.69–0.78 at 440 nm, 0.71–0.77 at 550 nm and 0.65–0.76 at 660
454 nm. This is on the low side of the range of values (0.73–0.93 at 550 nm) reported over West Africa
455 during DABEX for biomass burning plumes mixed with variable proportion of mineral dust
456 (*Johnson et al., 2008*). No clear tendency was found for the spectral dependence of SSA, which in
457 some of the cases decreased with wavelength and in others were very similar to each other at all
458 three wavelengths. The strongest spectral dependence of SSA was observed for biomass burning
459 plumes with the lowest absorption (highest SSA) at 440 nm. Laboratory experiments have shown
460 that strongly absorbing biomass burning particles tend to have a weak wavelength-dependent
461 absorption, while weakly light-absorbing particles tend to have a strong wavelength dependent
462 absorption (*McMeeking et al., 2014; Zhai et al., 2017*), which is consistent with results in this
463 study.

464

465 SSA values of anthropogenic pollution aerosols were generally intermediate in magnitude with
466 median values of 0.81 at 440 nm, 0.82 at 550 nm and 0.82 at 660 nm. Our data show that the value
467 of SSA varied significantly for the different plumes. Some pollution aerosols absorb almost as



468 strongly as biomass burning aerosols with SSA(550nm) values as low as 0.72, whereas the highest
469 SSA(550nm) value observed was 0.86. In addition, the absorption properties of urban aerosol
470 varied greatly between the sampled plumes for smoke of apparent same geographic origin. For
471 example, we measured SSA(550nm) values from 0.72 to 0.82 in the Accra pollution outflow. The
472 variability in SSA values may be due to the possible contribution of emissions from different cities
473 to the sampled pollution plumes (*Deroubaix et al., 2019*), thus having different combustion
474 sources and chemical ages. Past in-situ measurements of aerosol optical properties over SWA cities
475 appear, unfortunately, to be absent from literature. However, the flat spectral dependence of SSA
476 appears to be anomalous for anthropogenic pollution aerosols, as SSA is expected to decrease with
477 increasing wavelength (*Dubovick et al., 2002; Di Biagio et al., 2016*). As during DACCIWA SSAs
478 of anthropogenic pollution aerosols reached similar values to those of background aerosols, it
479 suggests a large contribution of the latter to the aerosol optical properties of the mixture.

480

481 The magnitude of SSA increased at the three wavelengths when dust events occurred. It is
482 important to note that the measurements exclude a significant portion of the coarse-mode aerosol
483 due to poor inlet passing efficiency of larger aerosol particles (a 50% size cut around 5 μm), which
484 may result in an overestimate of SSA. Despite this limitation, our measurements are comparable to
485 one another and to previous *in-situ* measurements by taking into account the sampling inlet. Large
486 variations in SSA were obtained with values ranging from 0.76–0.92 at 440 nm, 0.81–0.94 at 550
487 nm and 0.81–0.97 at 660 nm. Compared with the literature for transported dust, lower values were
488 obtained in the present study for few cases. For example, *Chen et al. (2011)* reported SSA(550 nm)
489 values of 0.97 ± 0.02 during NAMMA (a part of AMMA operated by NASA) using an inlet with a
490 comparable sampling efficiency. The lower values from DACCIWA reflect inherently more
491 absorbing aerosols in some dust plumes. In contrast to fire plumes, the SSA of dust aerosol showed
492 a clear increasing trend with wavelength. This behavior is likely due to the domination of large
493 particles in dust aerosol, which is in agreement to similar patterns observed in dust source regions
494 (*Dubovik et al., 2002*). Moreover, an increase of SSA is observed with wavelength for mixed dust-
495 smoke aerosol, suggesting that the aerosol particles were predominantly from dust, albeit mixed
496 with a significant loading of biomass burning.



497

		<i>SSA(450)</i>	<i>SSA(550)</i>	<i>SSA(660)</i>	<i>MEC(450)</i>	<i>MEC(550)</i>	<i>MEC(660)</i>	<i>g(450)</i>	<i>g(550)</i>	<i>g(660)</i>	<i>SAE</i>
Mineral dust	median	0.88	0.90	0.93	0.74	0.68	0.66	0.74	0.72	0.69	-0.35
	3 th	0.82	0.82	0.86	0.38	0.38	0.39	0.69	0.67	0.65	-0.56
	25 th	0.85	0.87	0.90	0.43	0.43	0.43	0.73	0.72	0.67	-0.48
	75 th	0.91	0.93	0.96	0.94	0.85	0.85	0.75	0.74	0.72	-0.25
	97 th	0.92	0.95	0.97	1.57	1.37	1.21	0.78	0.76	0.72	-0.12
Biomass burning	median	0.74	0.76	0.72	1.91	1.62	1.34	0.69	0.68	0.61	1.07
	3 th	0.70	0.72	0.66	0.94	1.45	1.22	0.64	0.65	0.59	0.59
	25 th	0.70	0.76	0.71	1.67	1.48	1.27	0.69	0.65	0.60	0.83
	75 th	0.77	0.77	0.74	1.86	1.65	1.55	0.72	0.68	0.62	1.15
	97 th	0.78	0.77	0.76	2.38	1.92	1.58	0.73	0.68	0.63	1.64
Mixed dust- Biomass burning	median	0.76	0.77	0.81	1.58	1.40	1.30	0.73	0.66	0.64	0.38
	3 th	-	-	-	-	-	-	-	-	-	-
	25 th	-	-	-	-	-	-	-	-	-	-
	75 th	-	-	-	-	-	-	-	-	-	-
	97 th	-	-	-	-	-	-	-	-	-	-
Anthropogenic Pollution	median	0.83	0.84	0.85	2.60	2.49	1.90	0.60	0.61	0.62	0.75
	3 th	0.78	0.79	0.81	0.70	1.24	0.54	0.60	0.59	0.54	0.30
	25 th	0.80	0.82	0.83	2.14	2.25	1.53	0.62	0.60	0.56	0.65
	75 th	0.84	0.86	0.85	3.51	2.96	2.53	0.69	0.62	0.67	0.89
	97 th	0.87	0.88	0.90	3.70	4.83	2.74	0.73	0.64	0.70	0.94

498

499 **Table 2. Single scattering albedo, extinction mass efficiency, asymmetry parameter, single**
 500 **scattering albedo and scattering Ångström exponent for the dominant aerosol classification.**

501

502 As shown in Table 2, the observed variability of *SSA* reflects a large variability for *MEC* at 550nm,
 503 which spans a wide range from 0.38 to 1.37 m² g⁻¹, 1.45 to 1.92 m² g⁻¹ and 1.24 to 4.83 m² g⁻¹ for
 504 dust, biomass burning for anthropogenic polluted aerosols, respectively. According to Mie theory,
 505 *MEC* is heavily influenced by the mass concentrations in the accumulation mode where the aerosol
 506 is optically more efficient in extinguishing radiation. We found *MEC* to be positively correlated
 507 with *SAE* (not shown) with measurement wavelengths (450–660 nm), which agrees with Mie
 508 theory. In contrast, the values of *g* appear to differ only little between the sampled plumes for a
 509 given aerosol class. We found *g* in the range of 0.67–0.76 for dust, 0.65–0.68 for biomass burning
 510 and 0.59–0.64 for anthropogenic polluted aerosols at 550 nm. *g* values in dust plumes were high,
 511 which is expected due to the presence of coarse particles contributing to forward scattering.

512

513 This analysis includes sampled aerosols originating from different source regions and having
 514 undergone different aging and mixing processes, which could explain some of the variability. The



515 impact of these factors on the magnitude and spectral dependence of optical parameters will be
516 investigated in the following section.

517

518 4. Discussion

519 4.1. Contribution of local anthropogenic pollution on aerosol absorption properties

520 Figure 6 shows the vertical distribution of *SSA*, *SAE* and *NO_x* mixing ratio for the dominant
521 aerosol classification. In dust plumes, if we exclude the case of mixing with biomass burning
522 aerosol, *SSAs* were fairly constant above 2.5 km amsl with values ranging between 0.90 and 0.93
523 at 550 nm, in agreement with values reported over dust source regions (*Schladitz et al., 2009*;
524 *Formenti et al., 2011*; *Ryder et al., 2013, 2018*). Despite the range of sources identified during
525 DACCIWA, dust absorption properties do not seem to be clearly linked to particle origin or time
526 of transport. Aerosols were more absorbing within the low-altitude dust plumes with *SSA* values
527 dropping to 0.81. *SAE* values exhibited simultaneously a sharp increase close to zero below 2.5 km
528 amsl. This is consistent with a higher concentration of fine particles, though the value of *SAE* was
529 still much lower than for pollution or background aerosol (i.e. where it is typically > 0.2), which
530 means that scattering was still dominated by larger particles. The decrease in *NO_x* with height
531 further indicates the concurrent influence by emissions from pollution sources in the low-altitude
532 dust plumes. Based on these observations, the strong variation in the light-absorption properties of
533 dust-dominated aerosol over SWA could be attributed to the degree of mixing into the vertical
534 column with either freshly emitted aerosols from urban/industrial sources or long-range
535 transported biomass burning aerosol.

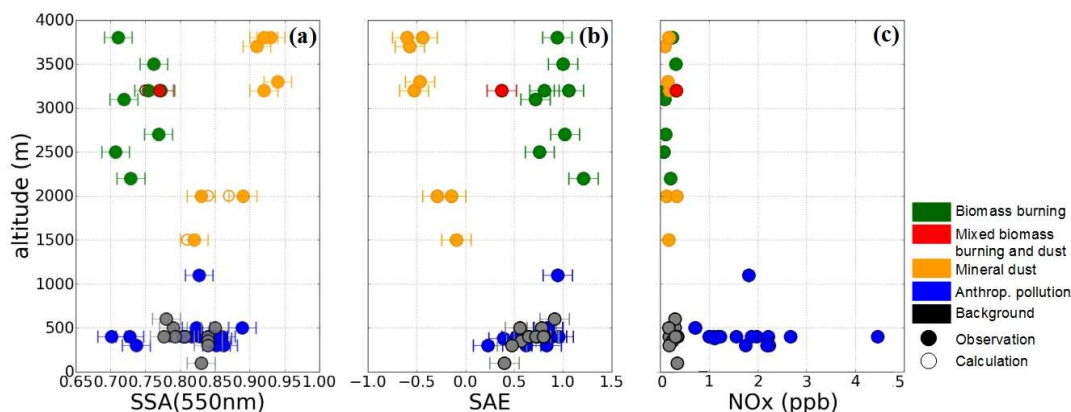
536

537 One of the critical factors in the calculation of aerosol direct and semi-direct radiative effects is the
538 mixing state of the aerosols, which can significantly affect absorbing properties. There were no
539 direct observational constraints available on this property during the DACCIWA airborne
540 campaign. However, we investigated the probable aerosol mixing state by calculating composite
541 *SSA* from the aerosol size distribution. On the basis of Figure 4, dust size distribution showed only
542 minor discrepancies in the mean and standard deviation of the coarse mode but significant
543 differences in the balance between fine and coarse modes, which suggests low internal mixing of
544 dust with other atmospheric species. The size distributions of mixed dust-pollution have been
545 deconvoluted by weighting the size distributions of mineral dust and anthropogenic pollution
546 aerosol averaged over the respective flights. This assumes that dust was externally mixed with the
547 anthropogenic pollution particles and assumes a homogeneous size distribution for the dust and
548 anthropogenic pollution aerosol throughout a flight. σ_{scat} and σ_{abs} were then calculated using Mie



549 theory from each composite size distributions and the corresponding k and m . The resulting σ_{scat}
550 and σ_{abs} were used to calculate a composite SSA . A similar calculation was performed for the mixed
551 dust-biomass burning case. Figure 6 shows a good agreement with the observations of SSA ,
552 implying that external mixing appears to be a reasonable assumption to compute aerosol direct and
553 semi-direct radiative effects in these dust layers for modeling applications. This is consistent with
554 the filter analysis performed during AMMA and SAMUM-2, which did not reveal any evidence of
555 internal mixing in both mixed dust-biomass burning and dust-anthropogenic pollution layers
556 (Chou *et al.*, 2008; Lieke *et al.*, 2011; Petzold *et al.*, 2011).

557



558 **Figure 6. Vertical distribution of (a) the single scattering albedo at 550 nm, (b) the scattering**
559 **Ångström exponent and (c) NOx mixing ratio for the dominant aerosol classification. In**
560 **panel (a), full circles represent SSA measurements and empty circles represent composite**
561 **SSA calculated by deconvoluting size distribution measurements in mixed dust layers and**
562 **assuming an external mixing state.**

563

564 Figure 6 indicates markedly different processes affecting optical properties of biomass burning
565 aerosols. SSA , SAE and NO_x of biomass burning plumes did not significantly vary with height
566 from 2.2 to 3.8 km amsl. Moreover, the size distribution of biomass burning aerosols for the
567 observed cases did not show significant contribution of ultrafine particles (Figure 4). These
568 observations seem to indicate that the absorption properties of biomass burning plumes were not
569 affected by direct pollution emissions, probably due to the remote location of the sampled biomass
570 burning plumes as discussed in section 3.2. The optical properties of aerosols are determined by
571 either the aerosol chemical composition, the aerosol size distribution, or both. Changes in the size
572 distribution of biomass burning aerosol due to coagulation and condensation have been shown to
573 alter the SSA , as particles increase towards sizes for which scattering is more efficient (Laing *et al.*,



574 2016). Variations in particle chemical composition, caused by source emissions and aging
575 processes associated with gas-to-particle transformation and internal mixing, has been shown to
576 change the *SSA* (Abel *et al.*, 2003; Petzold *et al.*, 2011). The contributions from size distribution
577 and chemical composition to the variation of *SSA* in biomass burning plumes will be explored in
578 section 4.2.

579

580 In the boundary layer, the similar *SSA* and *SAE* in anthropogenic pollution and background plumes
581 suggests that background aerosol may be rather called background pollution originating from a
582 regional background source in the far field. Our analysis of the spectral dependence of *SSA*
583 showed no apparent signature of anthropogenic pollution aerosols (see section 3.3) despite a strong
584 increase of aerosol number concentrations in air masses crossing urban centers (see section 3.2).
585 This can be explained by two factors: First, the majority of accumulation mode particles were
586 present in the background, while the large proportion of aerosols emitted from cities resided in the
587 ultrafine mode particles that have less scattering efficiencies (Figure 4). Second, large amounts of
588 absorbing aerosols in the background can minimize the impact of further increase of absorbing
589 particles to the aerosol load. We did not find any correlation between the values of *SSA* and their
590 spectral dependence, which suggests that the variability in *SSA* cannot be attributed to different
591 contributions of marine aerosol in pollution plumes. The high CO values (~180 ppb) observed in
592 background conditions further indicates a strong contribution of combustion emissions at the
593 surface. Recent studies showed a large background of biomass burning transported from the
594 Southern Hemisphere in SWA that dominated the aerosol chemical composition in the boundary
595 layer (Menut *et al.*, 2018; Haslett *et al.*, 2019). The high absorbing properties (*SSA*~0.81 at
596 550nm) of background aerosols is consistent with being a mixture of aged biomass burning and
597 Atlantic marine aerosol. Moreover *SSA* of background aerosol was lower than previously reported
598 over the Southern Atlantic (Ascension Island) outside the fire season in Central Africa (Zuidema
599 *et al.*, 2018), which supports this conclusion. These results highlight that aerosol optical properties at
600 the surface were dominated by the widespread biomass burning particles at regional scale.

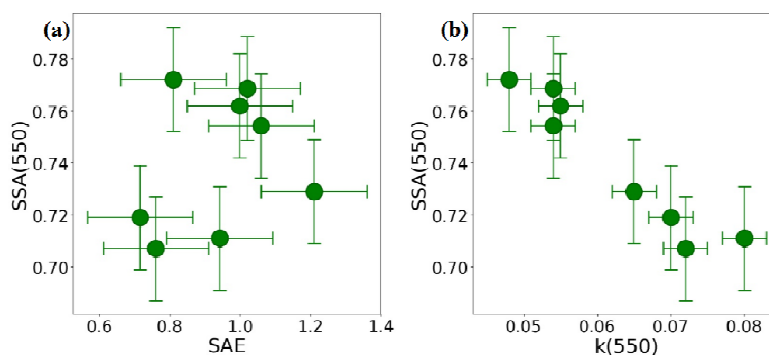
601

602 **4.2. Aging as a driver for absorption enhancement of biomass burning aerosol**

603 In order to determine the contributions from size distribution and chemical composition to the
604 variation of *SSA* in biomass burning plumes, *SSA* is presented as a function of *SAE* and *k* in Figure
605 7a and b, respectively. *k* was iteratively varied to reproduce the experimental scattering and
606 absorption coefficients, as described in section 2.3.1. It appears that the variation of the size
607 distribution (assessed via *SAE* in Figure 7a) had minimal impact in determining the variability of



608 SSA. Thus, the observations suggest that there was no effect of plume age on the size distribution,
609 consistent with previous observations of size distribution in aged biomass burning plumes
610 (Sakamoto *et al.*, 2015; Carrico *et al.*, 2016; Laing *et al.*, 2016). Using a Lagrangian
611 microphysical model, Sakamoto *et al.* (2015) have shown a rapid shift to larger sizes for biomass
612 burning plumes within the first hours of aging. Less drastic but similarly rapid growth by
613 coagulation was seen by Capes *et al.* (2008) in their box model. Given that the biomass burning
614 plumes sampled during DACCIWA had more than 5 days in age, the quick size-distribution
615 evolution within the early plume stages might explain the limited impact of the size distribution on
616 the SSA.



617
618 **Figure 7. Contribution to single scattering albedo (a) from particle size (assessed via SAE)**
619 **and (b) from composition (assessed via k) in biomass burning plumes.**
620

621 In contrast, Figure 7b shows that SSA variability was strongly influenced by the variability in
622 composition of biomass burning aerosol. Although there is some variability between the results
623 from different plumes, overall there was a consistent decrease in SSA with increasing k , implying a
624 high contribution for light-absorbing particles. The observed variability of SSA is reflected in a
625 large variability of k , which is estimated to span in the large range 0.048–0.080 at 550 nm. No
626 clear tendency was found for the wavelength dependence of k , which in some of the cases
627 increases with wavelength and in others decreases (not shown). Correspondingly, values of AAE in
628 biomass burning plumes ranged from 0.9 to 1.1 with a median value of 1.0. Theoretically, fine-
629 mode aerosol with absorption determined exclusively by BC would have AAE equal to 1.0, since
630 BC is expected to have a spectrally constant k (Bond *et al.*, 2013). Therefore, the low SSA values
631 observed in biomass burning plumes over SWA and the small spectral variation of k both suggest



632 that BC is the dominant absorber in the visible and near-IR wavelengths for these biomass burning
633 aerosols.

634

635 Compared with past in-situ measurements of aged biomass burning aerosol, *SSA* values over SWA
636 (0.71–0.77 at 550 nm) are at the lower end of those reported worldwide (0.73–0.99 at 550 nm)
637 (*Maggi et al., 2003; Reid et al. 2005; Johnson et al., 2008; Corr et al. 2012; Laing et al. 2016*).
638 This can be attributed in part to the high flaming versus smoldering conditions of African smoke
639 producing more BC particles (*Andreae and Merlet, 2001; Reid et al., 2005*), which inherently have
640 low *SSA* compared to other regions (*Dubovick et al. 2002*). However, *SSA* values over SWA are
641 significantly lower than the range reported near emission sources in sub-Saharan Africa and over
642 the southeast Atlantic, where values span over 0.84–0.90 at 550 nm (*Haywood et al., 2003b;*
643 *Pistone et al., 2019*). Recent observations carried out on Ascension Island to the south-west of the
644 DACCIWA region showed that smoke transported from Central and South African fires can be
645 very light absorbing over the July–November burning season but *SSA* values were still higher
646 (0.80 ± 0.02 at 530 nm; *Zuidema et al., 2018*) than those reported over SWA. A possible cause of
647 the lower *SSA* in SWA is that Ascension Island is much closer to the local sources and the aerosol
648 is therefore less aged.

649

650 Currently there are few field measurements of well-aged biomass burning emissions. Our
651 knowledge of biomass burning aerosol primarily comes from laboratory experiments and near-
652 field measurements taken within a few hours of a wildfire (*Abel et al., 2003; Yokelson et al., 2009;*
653 *Adler et al., 2011; Haywood et al., 2003b; Vakkari et al., 2014; Zhong and Jang, 2014; Forrister*
654 *et al., 2015; Laing et al., 2016; Zuidema et al., 2018*). Exception made of the study by *Zuidema*
655 *et al. (2018)* over the southeast Atlantic, it is generally found that the aged biomass burning aerosol
656 particles are less absorbing than freshly emitted aerosols due to a combination of condensation of
657 secondary organic species and an additional increase in size by coagulation. This is in contrast to
658 our results showing that *SSA* of biomass burning aerosols were significantly lower than directly
659 after emission and that the evolution of *SSA* occurred long time after emission.

660

661 There are three possible explanations for these results. First, one must consider sample bias. As
662 regional smoke ages, it can be enriched by smoke from other fires that can smolder for days
663 producing large quantities of non-absorbing particles, thereby increasing the mean *SSA* (*Reid et al.,*
664 *2005; Laing et al., 2016*). However, during DACCIWA, biomass burning plumes were transported
665 over the Atlantic Ocean and were probably less influenced by multiple fire emissions. Second,



666 there is evidence that fresh BC particles become coated with sulfate and organic species as the
667 plume ages in a manner that enhances their light absorption (*Lack et al., 2012; Schwarz et al.,*
668 *2008*). Finally, organic particles produced during the combustion phase can be lost during the
669 transport through photobleaching, volatilization and/or cloud-phase reactions (*Clarke et al., 2007;*
670 *Lewis et al., 2008; Forrister et al., 2015*), which is consistent with the low SSA and AAE values we
671 observed. Assessing whether these aging processes impact the chemical components and
672 henceforth optical properties of transported biomass burning aerosol would need extensive
673 investigation of aerosol chemical composition that will be carried out in a subsequent paper.

674

675 **5. Conclusions**

676 This paper provides an overview of *in-situ* airborne measurements of vertically resolved aerosol
677 optical properties carried out over SWA during the DACCIWA field campaign in June-July 2016.
678 The peculiar dynamics of the region lead to a chemically complex situation, which enabled
679 sampling various air masses, including long-range transport of biomass burning from Central
680 Africa and dust from Sahelian and Saharan sources, local anthropogenic plumes from the major
681 coastal cities, and mixtures of these different plumes. This work fills a research gap by providing,
682 firstly, key climate relevant aerosol properties (*SSA, MEC, g, SAE, AAE*) and secondly,
683 observations of the impact of aging and mixing processes on aerosols optical properties.

684

685 The aerosol vertical structure was very variable and mostly influenced by the origin of air mass
686 trajectories. While aerosol extinction coefficients generally decreased with height, there were
687 distinct patterns of profiles during dust and biomass burning transport to SWA. When present,
688 enhanced values of extinction coefficient up to 240 Mm^{-1} were observed in the 2–5 km amsl range.
689 These elevated aerosol layers were dominated by either dust or biomass burning aerosols, which is
690 consistent with what would be expected on the basis of the atmospheric circulations during the
691 monsoon season (*McConnell et al., 2008; Knippertz et al., 2017*). However, during one flight a
692 mixture of dust and biomass burning was found in a layer at around 3 km amsl, implying that there
693 may be substantial variability in the idealized picture. In the lower troposphere, the large
694 anthropogenic pollution plumes extended as far as hundreds of kilometers from the cities emission
695 sources and were not limited to the boundary layer but occurred also at higher levels up to 2.5 km
696 amsl, which is explained by vertical transport and mixing processes, partly triggered by the
697 orography of SWA (*Deroubaix et al., 2019; Flamant et al., 2018a*). The analysis of the aerosol size
698 distributions, SAE and NO_x suggests a strong mixing of dust with anthropogenic pollution
699 particles in dust layers transported below 2.5 km amsl, whereas biomass burning plumes that were



700 transported more northward were not affected by this mixing. Both transport pathways and vertical
701 structures of biomass burning and dust plumes over SWA appear to be the main factors affecting
702 the mixing of anthropogenic pollution with dust and biomass burning particles.

703

704 The aerosol light absorption in dust plumes was strongly enhanced as the result of this mixing. We
705 find a decrease of $SSA(550nm)$ from 0.92 to 0.81 for dust affected by anthropogenic pollution
706 mixing compared to the situation in which the dust plumes moved at higher altitudes across SWA.
707 Comparison of the particle size distributions of the different dust plumes showed a large
708 contribution of externally mixed fine mode particles in mixed layers, while there was no evidence
709 for internal mixing of coarse particles. Concurrent optical calculations by deconvoluting size
710 distribution measurements in mixed layers and assuming an external mixing state allowed to
711 reproduce the observed $SSAs$. This implies that an external mixing would be a reasonable
712 assumption to compute aerosol direct and semi-direct radiative effects in mixed dust layers.

713

714 Despite a strong increase of aerosol number concentration in air masses crossing urban
715 conglomerations, the magnitude of the spectral $SSAs$ was comparable to the background.
716 Enhancements of light absorption properties were seen in some pollution plumes, but were not
717 statistically significant. A persistent spectral signature of biomass burning aerosols in both
718 background and pollution plumes highlights that the aerosol optical properties in the boundary
719 layer were strongly affected by the ubiquitous biomass burning aerosols transported from Central
720 Africa (*Menut et al., 2018; Haslett et al., 2019*). The large proportion of aerosols emitted from
721 cities that resided in the ultrafine mode particles have limited impact on already elevated amounts
722 of accumulation mode particles having a maximal absorption efficiency. As a result, in the
723 boundary layer, the contribution from local city emissions to aerosol optical properties were of
724 secondary importance at regional scale compared with this large absorbing aerosol mass. While
725 local anthropogenic emissions are expected to rise as SWA is currently experiencing major
726 economic and population growth, there is increasing evidence that climate change is increasing the
727 frequency and distribution of fire events (*Joly et al., 2015*). In terms of future climate scenarios
728 and accompanying aerosol radiative forcing, whether the large biomass burning events that occur
729 during the monsoon season would limit the radiative impact of increasing anthropogenic
730 emissions, remains an open and important question.

731



732 The SSA values of biomass burning aerosols transported in the free troposphere were very low
733 (0.71–0.77 at 550 nm) and have only rarely been observed in the atmosphere. The variability in
734 SSA was mainly controlled by the variability in aerosol composition (assessed via k) rather than by
735 variations in the aerosol size distribution. Correspondingly, values of AAE ranged from 0.9 to 1.1,
736 suggesting that BC particles were the dominant absorber in the visible for these biomass burning
737 aerosols. In recent years the southern Atlantic Ocean, especially the area of the west coast of
738 Africa, became an increasing focus in the research community, through the ORACLES/LASIC
739 (ObseRvations of Aerosols above CLouds and their intEractionS/Layered Atlantic Smoke
740 Interactions with Clouds), AEROCLO-sA (AErosol RadiatiOn and CLOuds in Southern Africa –
741 AEROCLO-SA) and CLARIFY (Cloud and Aerosols Radiative Impact and Forcing) projects
742 (Zuidema *et al.*; 2016; Zuidema *et al.*; 2018; Formenti *et al.*; 2019). Comparison with literature
743 showed a consistent picture of increasing absorption enhancement of biomass burning aerosol
744 from emission to remote locations. Further, the range of SSA values over SWA was slightly lower
745 than that reported on Ascension Island to the south-west of the DACCIWA region, which
746 underscores that the evolution of SSA occurred long time after emission. While the mechanism
747 responsible for this phenomenon warrants further study, our results support the growing body of
748 evidence that the optical parameters used in regional/global climate modeling studies, especially
749 absorption by biomass burning aerosols, have to be better constrained using these recent
750 observations to determine the direct and semi-direct radiative effects of smoke particles over this
751 region (Mallet *et al.* 2019). In particular and regarding the very high absorbing properties of
752 smoke, specific attention should be dedicated to the semi-direct effect of biomass burning aerosols
753 at the regional scale and its relative contribution to the indirect radiative effect.

754

755 We believe the set of DACCIWA observations presented here is representative of the regional
756 mean and variability in aerosol optical properties that can be observed during the monsoon season
757 over SWA, as the main dynamical features were in line with climatology (Knippertz *et al.*, 2017).
758 This is why results from the present study will serve as input and constraints for climate modeling
759 to better understand the impact of aerosol particles on the radiative balance and cloud properties
760 over this region and also will substantially support remote sensing retrievals.



761 *Data availability.*

762 All data used in this study are publicly available on the AERIS Data and Service Center, which can
763 be found at <http://baobab.sedoo.fr/DACCIWA>.

764

765 *Author contributions.*

766 CD conducted the analysis of the data and wrote the paper. CD, TB, FB, NM, AC, PD, JB, RD, KS
767 and AS operated aircraft instruments and processed and/or quality-controlled data. MM provided
768 expertise on aerosol-climate interaction processes. CF and PK were PIs, who led the funding
769 application and coordinated the DACCIWA field campaign. All co-authors contributed to the
770 writing of the paper.

771

772 *Acknowledgements.*

773 The research leading to these results has received funding from the European Union 7th
774 Framework Programme (FP7/2007-2013) under Grant Agreement no. 603502 (EU project
775 DACCIWA: Dynamics-aerosol-chemistry-cloud interactions in West Africa). The European
776 Facility for Airborne Research (EUFAR, <http://www.eufar.net/>) also supported the project through
777 the funding of the Transnational Activity project OLACTA and MICWA. We thank the Service des
778 Avions Français Instrumentés pour la Recherche en Environnement (SAFIRE, a joint entity of
779 CNRS, Météo-France, and CNES) and operator of the ATR-42 for their support during the aircraft
780 campaign. Cyrielle Denjean thanks CNES for financial support. The authors would like to thank
781 Bruno Piguet (CNRM) and Michel Ramonet (LSCE) for their support in the data processing.



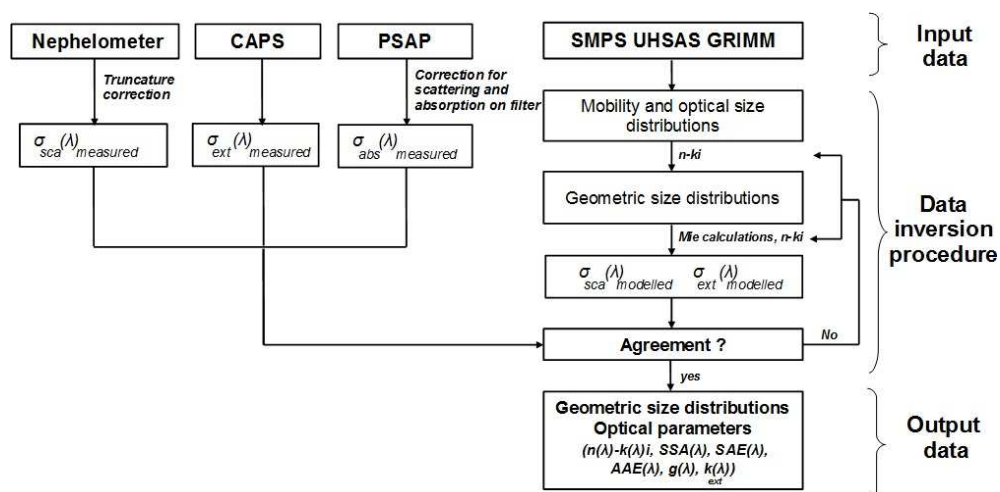
782 **Appendix 1. Summary of flight information. All flights were conducted during 2016.**

Flight number	Date	Take off time (UTC)	Landing time (UTC)	Events observed
F17	29 June	14:17	17:10	Export of pollution from Lomé
F18	30 June	12:52	16:29	Export of pollution from Lomé
F19	1 July	10:35	14:06	Export of pollution from Accra
F20	2 July	09:53	13:21	Export of pollution from Lomé Dust outbreak
F21	2 July	15:04	18:29	Export of pollution from Lomé Biomass burning outbreak Mixed dust-biomass burning outbreak
F22	3 July	09:54	13:29	Export of pollution from Lomé
F24	6 July	07:17	11:03	Export of pollution from Abidjan
F27	8 July	05:52	09:28	Export of pollution from Accra
F28	8 July	10:53	14:22	Dust outbreak
F29	10 July	10:31	14:11	Export of pollution from Lomé Dust outbreak
F30	11 July	07:19	11:01	Export of pollution from Abidjan Biomass burning outbreak
F31	11 July	13:48	16:42	Biomass burning outbreak
F32	12 July	13:56	17:20	Export of pollution from Accra
F33	13 July	12:40	16:11	Biomass burning outbreak
F35	15 July	09:32	13:00	Export of pollution from Lomé

783



784 **Appendix 2. Data inversion procedure to calculate the aerosol microphysical and optical**
 785 **parameters.**



786



787 **References**

- 788 Abel, S. J., Haywood, J. M., Highwood, E. J., Li, J., and Buseck, P. R.: Evolution of biomass
789 burning aerosol properties from an agricultural fire in southern Africa, *Geophys. Res. Lett.*, 30,
790 1783, doi:10.1029/2002GL017342, 2003.
- 791 Adler, G., Flores, J. M., Abo Riziq, A., Borrmann, S., and Rudich, Y., Chemical, physical, and
792 optical evolution of biomass burning aerosols: a case study, *Atmos. Chem. Phys.*, 11, 1491-
793 1503, <https://doi.org/10.5194/acp-11-1491-2011>, 2011.
- 794 Andreae, M.O. and Merlet, P., Emission of Trace Gases and Aerosols from Biomass Burning.
795 *Global Biogeochemical Cycles*, 15, 955-966, 2001.
- 796 Ansmann, A., Petzold, A., Kandler, K., Tegen, I. N. A., Wendisch, M., Müller, D., Weinzierl, B.,
797 Müller, T., and Heintzenberg, J.: Saharan Mineral Dust Experiments SAMUM-1 and
798 SAMUM-2: what have we learned?, *Tellus B*, 63, 403-429, doi: 10.1111/j.1600-
799 0889.2011.00555.x, 2011.
- 800 Bond, T. C., Doherty, S. J., Fahey, D. W., Forster, P. M., Berntsen, T., DeAngelo, B. J., Flanner, M.
801 G., Ghan, S., Kärcher, B., Koch, D., Kinne, S., Kondo, Y., Quinn, P. K., Sarofim, M. C.,
802 Schultz, M. G., Schulz, M., Venkataraman, C., Zhang, H., Zhang, S., Bellouin, N., Guttikunda, S.
803 K., Hopke, P. K., Jacobson, M. Z., Kaiser, J. W., Klimont, Z., Lohmann, U., Schwarz, J. P.,
804 Shindell, D., Storelvmo, T., Warren, S. G., and Zender, C. S.: Bounding the role of black carbon
805 in the climate system: A scientific assessment, *J. Geophys. Res.*, 118, 1-173,
806 doi:10.1002/jgrd.50171, 2013.
- 807 Boucher, O., D. Randall, P. Artaxo, C. Bretherton, G. Feingold, P. Forster, V.-M. Kerminen, Y.
808 Kondo, H. Liao, U. Lohmann, P. Rasch, S.K. Satheesh, S. Sherwood, B. Stevens, and X.Y.
809 Zhang: Clouds and aerosols. In *Climate Change 2013: The Physical Science Basis*.
810 Contribution of Working Group I to the Fifth Assessment Report of the Intergovernmental
811 Panel on Climate Change. T.F. Stocker, D. Qin, G.-K. Plattner, M. Tignor, S.K. Allen, J.
812 Doschung, A. Nauels, Y. Xia, V. Bex, and P.M. Midgley, Eds. Cambridge University Press, pp.
813 571-657, doi:10.1017/CBO9781107415324.016, 2013.
- 814 Capes, G., B. Johnson, G. McFiggans, P. I. Williams, J. M. Haywood, and H. Coe, Aging of
815 biomass burning aerosols over West Africa: Aircraft measurements of chemical composition,
816 microphysical properties and emission ratios, *J. Geophys. Res.*, 113, D00C15,
817 doi:10.1029/2008JD009845, 2008.
- 818 Carrico, C.M., Prenni, A.J., Kreidenweis, S.M., Levin, E.J., McCluskey, C.S., DeMott, P.J.,
819 McMeeking, G.R., Rapidly evolving ultrafine and fine mode biomass smoke physical



- 820 properties: comparing laboratory and field results, *J. Geophys. Res. Atmos.*, 121(10),
821 10.1002/2015JD024389, 2016.
- 822 Chen, G., Ziemba, L. D., Chu, D. A., Thornhill, K. L., Schuster, G. L., Winstead, E. L., Diskin, G.
823 S., Ferrare, R. A., Burton, S. P., Ismail, S., Kooi, S. A., Omar, A. H., Slusher, D. L., Kleb, M.
824 M., Reid, J. S., Twohy, C. H., Zhang, H., and Anderson, B. E.: Observations of Saharan dust
825 microphysical and optical properties from the Eastern Atlantic during NAMMA airborne field
826 campaign, *Atmos. Chem. Phys.*, 11, 723-740, <https://doi.org/10.5194/acp-11-723-2011>, 2011.
- 827 Chou, C., P. Formenti, M. Maille, P. Ausset, G. Helas, S. Osborne, and M. Harrison, Size
828 distribution, shape and composition of dust aerosols collected during the AMMA SOP0 field
829 campaign in the northeast of Niger, January 2006, *J. Geophys. Res.*, 113, D00C10,
830 doi:10.1029/2008JD009897, 2008.
- 831 Clarke, A., McNaughton, C., Kapustin, V., Shinozuka, Y., Howell, S., Dibb, J., Zhou, J., Anderson,
832 B., Brekhovskikh, V., Turner, H., and Pinkerton, M.: Biomass burning and pollution aerosol
833 over North America: organic components and their influence on spectral optical properties and
834 humidification response, *J. Geophys. Res.*, 112, D12S18, doi:10.1029/2006JD007777, 2007.
- 835 Corr, C. A., Hall, S. R., Ullmann, K., Anderson, B. E., Beyersdorf, A. J., Thornhill, K. L., Cubison,
836 M. J., Jimenez, J. L., Wisthaler, A., and Dibb, J. E.: Spectral absorption of biomass burning
837 aerosol determined from retrieved single scattering albedo during ARCTAS, *Atmos. Chem.*
838 *Phys.*, 12, 10505-10518, <https://doi.org/10.5194/acp-12-10505-2012>, 2012.
- 839 Deetz, K., Vogel, H., Haslett, S., Knippertz, P., Coe, H., and Vogel, B.: Aerosol liquid water
840 content in the moist southern West African monsoon layer and its radiative impact, *Atmos.*
841 *Chem. Phys.*, 18, 14271-14295, <https://doi.org/10.5194/acp-18-14271-2018>, 2018.
- 842 Denjean, C., Cassola, F., Mazzino, A., Triquet, S., Chevaillier, S., Grand, N., Bourriane, T.,
843 Momboisse, G., Sellegri, K., Schwarzenbock, A., Freney, E., Mallet, M., and Formenti, P.: Size
844 distribution and optical properties of mineral dust aerosols transported in the western
845 Mediterranean, *Atmos. Chem. Phys.*, 16, 1081-1104, <https://doi.org/10.5194/acp-16-1081-2016>,
846 2016.
- 847 Deroubaix, A., Menut, L., Flamant, C., Brito, J., Denjean, C., Dreiling, V., Fink, A., Jambert, C.,
848 Kalthoff, N., Knippertz, P., Ladkin, R., Mailler, S., Maranan, M., Pacifico, F., Piguet, B., Siour,
849 G., and Turquety, S.: Diurnal cycle of coastal anthropogenic pollutant transport over southern
850 West Africa during the DACCIWA campaign, *Atmos. Chem. Phys.*, 19, 473-497,
851 <https://doi.org/10.5194/acp-19-473-2019>, 2019.
- 852 Di Biagio, C., Formenti, P., Doppler, L., Gaimoz, C., Grand, N., Ancellet, G., Attié, J.-L., Bucci,
853 S., Dubuisson, P., Fierli, F., Mallet, M., and Ravetta, F.: Continental pollution in the Western



- 854 Mediterranean basin: large variability of the aerosol single scattering albedo and influence on
855 the direct shortwave radiative effect, *Atmos. Chem. Phys.*, 16, 10591-10607,
856 <https://doi.org/10.5194/acp-16-10591-2016>, 2016.
- 857 Dubovik, O., Holben, B. N., Eck, T. F., Smirnov, A., Kaufman, Y. J., King, M. D., Tanre, D., and
858 Slutsker, I.: Climatology of atmospheric aerosol absorption and optical properties in key
859 locations, *J. Atmos. Sci.*, 59, 590–608, 2002.
- 860 Flamant, C., Deroubaix, A., Chazette, P., Brito, J., Gaetani, M., Knippertz, P., Fink, A. H., de
861 Coetlogon, G., Menut, L., Colomb, A., Denjean, C., Meynadier, R., Rosenberg, P., Dupuy, R.,
862 Dominutti, P., Duplissy, J., Bourriane, T., Schwarzenboeck, A., Ramonet, M., and Totems, J.:
863 Aerosol distribution in the northern Gulf of Guinea: local anthropogenic sources, long-range
864 transport, and the role of coastal shallow circulations, *Atmospheric Chemistry and Physics*, 18,
865 12 363–12 389, <https://doi.org/10.5194/acp-18-12363-2018>, 2018a.
- 866 Flamant C., Knippertz, P., Fink, A. H., Akpo, A., Brooks, B., Chiu, C. J., Coe, H., Danuor, S.,
867 Evans, M., Jegede, O., Kalthoff, N., Konaré, A., Liousse, C., Lohou, F., Mari, C., Schlager, H.,
868 Schwarzenboeck, A., Adler, B., Amekudzi, L., Aryee, J., Ayoola, M., Batenburg, A. M.,
869 Bessardon, G., Borrmann, S., Brito, J., Bower, K., Burnet, F., Catoire, V., Colomb, A., Denjean,
870 C., Fosu-Amankwah, K., Hill, P. G., Lee, J., Lathon, M., Maranan, M., Marsham, J.,
871 Meynadier, R., Ngamini, J.-B., Rosenberg, P., Sauer, D., Smith, V., Stratmann, G., Taylor, J. W.,
872 Voigt, C., and Yoboué, V.: The Dynamics-Aerosol-Chemistry-Cloud Interactions in West Africa
873 field campaign: Overview and research highlights, *B. Am. Meteorol. Soc.*, 99, 83–104,
874 <https://doi.org/10.1175/BAMS-D-16-0256.1>, 2018b.
- 875 Formenti, P., Rajot, J. L., Desboeufs, K., Saïd, F., Grand, N., Chevaillier, S., and Schmechtig, C.:
876 Airborne observations of mineral dust over western Africa in the summer Monsoons season:
877 spatial and vertical variability of physico-chemical and optical properties, *Atmos. Chem. Phys.*,
878 11, 6387–6410, doi:10.5194/acp-11-6387-2011, 2011.
- 879 Formenti, P., B. D'Anna, C. Flamant, M. Mallet, S.J. Piketh, K. Schepanski, F. Waquet, F. Auriol,
880 G. Brogniez, F. Burnet, J. Chaboureaud, A. Chauvigné, P. Chazette, C. Denjean, K. Desboeufs, J.
881 Doussin, N. Elguindi, S. Feuerstein, M. Gaetani, C. Giorio, D. Klopper, M.D. Mallet, P. Nabat,
882 A. Monod, F. Solmon, A. Namwoonde, C. Chikwililwa, R. Mushi, E.J. Welton, and B. Holben,
883 O: The Aerosols, Radiation and Clouds in southern Africa (AERO-CLO-SA) field campaign in
884 Namibia: overview, illustrative observations and way forward. *Bull. Amer. Meteor. Soc.*, 0,
885 <https://doi.org/10.1175/BAMS-D-17-0278.1>, 2019.



- 886 Forrister, H., Liu, J., Scheuer, E., Dibb, J., Ziemba, L., Thornhill, K. L., Anderson, B., Diskin, G.,
887 Perring, A. E., and Schwarz, J. P.: Evolution of brown carbon in wildfire plumes, *Geophys.*
888 *Res. Lett.*, 42, 4623–4630, 2015.
- 889 Haslett, S. L., Taylor, J. W., Evans, M., Morris, E., Vogel, B., Dajuma, A., Brito, J., Batenburg, A.
890 M., Borrmann, S., Schneider, J., Schulz, C., Denjean, C., Bourrienne, T., Knippertz, P., Dupuy,
891 R., Schwarzenböck, A., Sauer, D., Flamant, C., Dorsey, J., Crawford, I., and Coe, H.: Remote
892 biomass burning dominates southern West African air pollution during the monsoon, *Atmos.*
893 *Chem. Phys. Discuss.*, <https://doi.org/10.5194/acp-2019-38>, in review, 2019.
- 894 Haywood, J. M., Francis, P., Osborne, S., Glew, M., Loeb, N., Highwood, E., Tanre, D., Myhre, G.,
895 Formenti, P., and Hirst, E.: Radiative properties and direct radiative effect of Saharan dust
896 measured by the C-130 aircraft during SHADE:1. Solar spectrum, *J. Geophys. Res.-Atmos.*,
897 108, 8577, <https://doi.org/10.1029/2002jd002687>, 2003a.
- 898 Haywood, J. M., S. R. Osborne, P. N. Francis, A. Keil, P. Formenti, M. O. Andreae, and P. H. Kaye,
899 The mean physical and optical properties of regional haze dominated by biomass burning
900 aerosol measured from the C-130 aircraft during SAFARI 2000, *J. Geophys. Res.*, 108(D13),
901 8473, doi:10.1029/2002JD002226, 2003b.
- 902 Haywood, J. M., Pelon, J., Formenti, P., Bharmal, N., Brooks, M., et al.: Overview of the dust and
903 biomass-burning experiment and African Monsoon multidisciplinary analysis special observing
904 period-0., *J. Geophys. Res.*, 113, doi:10.1029/2008JD010077, 2008.
- 905 Heintzenberg, J., The SAMUM-1 experiment over Southern Morocco: Overview and introduction,
906 *Tellus Ser. B*, 61, 2-11, 2009.
- 907 Hess, M., Koepke, P., Schult I., Optical properties of aerosols and clouds, *Bull. Amer. Meteor.*
908 *Soc.*, 79, 831-844, 1998.
- 909 Janhäll, S., Andreae, M. O., and Pöschl, U.: Biomass burning aerosol emissions from vegetation
910 fires: particle number and mass emission factors and size distributions, *Atmos. Chem. Phys.*,
911 10, 1427-1439, <https://doi.org/10.5194/acp-10-1427-2010>, 2010.
- 912 Johnson, B. T., Heese, B., McFarlane, S. A., Chazette, P., Jones, A. et al.: Vertical distribution and
913 radiative effects of mineral dust and biomass burning aerosol over West Africa during DABEX,
914 *J. Geophys. Res.*, 113(D17), D00C12, doi:10.1029/2008JD009848, 2008.
- 915 Jolly, W. M., Cochrane, M. A., Freeborn, P. H., Holden, Z. A., Brown, T. J., Williamson, G. J., and
916 Bowman, D. M. J. S.: Climate-induced variations in global wild- fire danger from 1979 to
917 2013, *Nat. Commun.*, 6, 7537, <https://doi.org/10.1038/ncomms8537>, 2015.
- 918 Kalthoff, N., Lohou, F., Brooks, B., Jegede, G., Adler, B., Babić, K., Dione, C., Ajao, A.,
919 Amekudzi, L. K., Aryee, J. N. A., Ayoola, M., Bessardon, G., Danuor, S. K., Handwerker, J.,



- 920 Kohler, M., Lothon, M., Pedruzo-Bagazgoitia, X., Smith, V., Sunmonu, L., Wieser, A., Fink, A.
921 H., and Knippertz, P.: An overview of the diurnal cycle of the atmospheric boundary layer
922 during the West African monsoon season: results from the 2016 observational campaign,
923 *Atmos. Chem. Phys.*, 18, 2913–2928, <https://doi.org/10.5194/acp-18-2913-2018>, 2018.
- 924 Kirchstetter T. W. , Novakov, T., and Hobbs, P.: Evidence that the spectral dependence of light
925 absorption by aerosols is affected by organic carbon, *J. Geophys. Res.*, 109,
926 D21208, doi:10.1029/2004JD004999, 2004.
- 927 Knippertz, P., Evans, M. J., Field, P. R., Fink, A. H., Liousse, C., and Marsham, J. H.: The possible
928 role of local air pollution in climate change in West Africa, *Nat. Clim. Change*, 5, 815–822,
929 <https://doi.org/10.1038/nclimate2727>, 2015a.
- 930 Knippertz, P., Coe, H., Chiu, J. C., Evans, M. J., Fink, A. H., Kalthoff, N., Liousse, C., Mari, C.,
931 Allan, R. P., Brooks, B., Danour, S., Flamant, C., Jegede, O. O., Lohou, F., and Marsham, J. H.:
932 The daccwa project: Dynamics-Aerosol- Chemistry-Cloud Interactions in West Africa, *Bulletin*
933 *of the American Meteorological Society*, 96, 1451–1460, [https://doi.org/10.1175/BAMS-D-14-](https://doi.org/10.1175/BAMS-D-14-00108.1)
934 [00108.1](http://journals.ametsoc.org/doi/10.1175/BAMS-D-14-00108.1), <http://journals.ametsoc.org/doi/10.1175/BAMS-D-14-00108.1>, 2015b.
- 935 Knippertz, P., Fink, A. H., Deroubaix, A., Morris, E., Tocquer, F., Evans, M. J., Flamant, C.,
936 Gaetani, M., Lavaysse, C., Mari, C., Marsham, J. H., Meynadier, R., Affo-Dogo, A., Bahaga,
937 T., Brosse, F., Deetz, K., Guebsi, R., Latifou, I., Maranan, M., Rosenberg, 5 P. D., and
938 Schlueter, A.: A meteorological and chemical overview of the DACCIWA field campaign in
939 West Africa in June–July 2016, *Atmospheric Chemistry and Physics*, 17, 10 893–10 918,
940 <https://www.atmos-chem-phys.net/17/10893/2017/>, 2017.
- 941 Lack, D. A. and Cappa, C. D.: Impact of brown and clear carbon on light absorption enhancement,
942 single scatter albedo and absorption wavelength dependence of black carbon, *Atmos. Chem.*
943 *Phys.*, 10, 4207–4220, doi:10.5194/acp-10-4207-2010, 2010.
- 944 Laing, J. R., Jaffe, D. A., and Hee, J. R.: Physical and optical properties of aged biomass burning
945 aerosol from wildfires in Siberia and the Western USA at the Mt. Bachelor Observatory, *Atmos.*
946 *Chem. Phys.*, 16, 15185–15197, <https://doi.org/10.5194/acp-16-15185-2016>, 2016.
- 947 Lebel, T., Parker, D.J., Flamant, C., Bourles, B., Marticorena, M., Mougin, E., Peugeot, C.,
948 Diedhiou, A., Haywood, J.M., Ngamini, J.B., Polcher, J., Redelsperger, J.L., Thorncroft, C.D.:
949 The AMMA field campaigns: multiscale and multidisciplinary observations in the West African
950 region, *Quarterly Journal of the Royal Meteorological Society*, 136(S1), 8–33, 2010.
- 951 Lewis, K., Arnott, W. P., Moosmuller, H., and Wold, C. E.: Strong spectral variation of biomass
952 smoke light absorption and single scattering albedo observed with a novel dual-wavelength
953 photoacoustic instrument, *J. Geophys. Res.*, 113, D16203, doi:10.1029/2007jd009699, 2008.



- 954 Lieke, K., Kandler, K., Scheuven, D., Emmel, C., Von Glahn, C., Petzold, A., Weinzierl, B., Veira,
955 A., Ebert, M., Weinbruch, S., and SchÜTZ, L.: Particle chemical properties in the vertical
956 column based on aircraft observations in the vicinity of Cape Verde Islands, *Tellus B*, 63, 497-
957 511, doi: 10.1111/j.1600-0889.2011.00553.x, 2011.
- 958 Liousse, C., Assamoi, E., Criqui, P., Granier, C., and Rosset, R.: Explosive growth in African
959 combustion emissions from 2005 to 2030, *Environmental Research Letters*, 9, 035003,
960 <https://doi.org/10.1088/1748-9326/9/3/035003>, 2014.
- 961 Liu, D., Taylor, J. W., Crosier, J., Marsden, N., Bower, K. N., Lloyd, G., Ryder, C. L., Brooke, J.
962 K., Cotton, R., Marengo, F., Blyth, A., Cui, Z., Estelles, V., Gallagher, M., Coe, H., and
963 Choularton, T. W.: Aircraft and ground measurements of dust aerosols over the west African
964 coast in summer 2015 during ICE-D and AER-D, *Atmos. Chem. Phys.*, 18, 3817-3838,
965 <https://doi.org/10.5194/acp-18-3817-2018>, 2018.
- 966 Magi, B. I., Magi A., Hobbs P.V., Schmid B., and Redemann J., Vertical profiles of light scattering,
967 light absorption and single-scattering albedo during the dry, biomass burning season in
968 southern Africa and comparisons of in situ and remote sensing measurements of aerosol optical
969 depths, *Journal of Geophysical Research*, 108 (D13), doi:10.1029/2002JD002361, 2003.
- 970 Mallet, M., Nabat, P., Zuidema, P., Redemann, J., Sayer, A. M., Stengel, M., Schmidt, S.,
971 Cochrane, S., Burton, S., Ferrare, R., Meyer, K., Saide, P., Jethva, H., Torres, O., Wood, R.,
972 Saint Martin, D., Roehrig, R., Hsu, C., and Formenti, P.: Simulation of the transport, vertical
973 distribution, optical properties and radiative impact of smoke aerosols with the ALADIN
974 regional climate model during the ORACLES-2016 and LASIC experiments, *Atmos. Chem.*
975 *Phys.*, 19, 4963-4990, <https://doi.org/10.5194/acp-19-4963-2019>, 2019.
- 976 Mann, G. W., Carslaw, K. S., Reddington, C. L., Pringle, K. J., Schulz, M., Asmi, A., Spracklen, D.
977 V., Ridley, D. A., Woodhouse, M. T., Lee, L. A., Zhang, K., Ghan, S. J., Easter, R. C., Liu, X.,
978 Stier, P., Lee, Y. H., Adams, P. J., Tost, H., Lelieveld, J., Bauer, S. E., Tsigaridis, K., van Noije,
979 T. P. C., Strunk, A., Vignati, E., Bellouin, N., Dalvi, M., Johnson, C. E., Bergman, T., Kokkola,
980 H., von Salzen, K., Yu, F., Luo, G., Petzold, A., Heintzenberg, J., Clarke, A., Ogren, J. A., Gras,
981 J., Baltensperger, U., Kaminski, U., Jennings, S. G., O'Dowd, C. D., Harrison, R. M., Beddows,
982 D. C. S., Kulmala, M., Viisanen, Y., Ulevicius, V., Mihalopoulos, N., Zdimal, V., Fiebig, M.,
983 Hansson, H.-C., Swietlicki, E., and Henzing, J. S.: Intercomparison and evaluation of global
984 aerosol microphysical properties among AeroCom models of a range of complexity, *Atmos.*
985 *Chem. Phys.*, 14, 4679-4713, <https://doi.org/10.5194/acp-14-4679-2014>, 2014.
- 986 Mari, C. H., Cailley, G., Corre, L., Saunois, M., Attié, J. L., Thouret, V., and Stohl, A.: Tracing
987 biomass burning plumes from the Southern Hemisphere during the AMMA 2006 wet season



- 988 experiment, *Atmos. Chem. Phys.*, 8, 3951-3961, <https://doi.org/10.5194/acp-8-3951-2008>,
989 2008.
- 990 Martinorena, B. and Bergametti, G.: Two-year simulations of seasonal and interannual changes of
991 the Saharan dust emissions, *Geophys. Res. Lett.*, 23, 1921-1924, 1996.
- 992 McConnell, C. L., Highwood, E. J., Coe, H., Formenti, P., Anderson, B., Osborne, S., Nava, S.,
993 Desboeufs, K., Chen, G., and Harrison, M. A. J.: Seasonal variations of the physical and optical
994 characteristics of Saharan dust: Results from the Dust Outflowand Deposition to the Ocean
995 (DODO) experiment, *J. Geophys. Res.*, 113, D14S05, doi:10.1029/2007JD009606, 2008.
- 996 McMeeking, G. R., Fortner, E., Onasch, T. B., Taylor, J. W. Flynn, M., Coe, H., and Kreidenweis,
997 S. M.: Impacts of non-refractory material on light absorption by aerosols emitted from biomass
998 burning, *J. Geophys. Res.-Atmos.*, 119, 2014JD021750,
999 <https://doi.org/10.1002/2014JD021750>, 2014.
- 1000 Menut, L., Flamant, C., Turquety, S., Deroubaix, A., Chazette, P., and Meynadier, R.: Impact of
1001 biomass burning on pollutant surface concentrations in megacities of the Gulf of Guinea,
1002 *Atmospheric Chemistry and Physics*, 18, 2687–20 2707, [https://doi.org/10.5194/acp-18-2687-](https://doi.org/10.5194/acp-18-2687-2018)
1003 2018, 2018.
- 1004 Myhre, G., Samset, B. H., Schulz, M., Balkanski, Y., Bauer, S., Berntsen, T. K., Bian, H., Bellouin,
1005 N., Chin, M., Diehl, T., Easter, R. C., Feichter, J., Ghan, S. J., Hauglustaine, D., Iversen, T.,
1006 Kinne, S., Kirkevåg, A., Lamarque, J.-F., Lin, G., Liu, X., Lund, M. T., Luo, G., Ma, X., van
1007 Noije, T., Penner, J. E., Rasch, P. J., Ruiz, A., Seland, Skeie, R. B., Stier, P., Takemura, T.,
1008 Tsigaridis, K., Wang, P., Wang, Z., Xu, L., Yu, H., Yu, F., Yoon, J.-H., Zhang, K., Zhang, H.,
1009 and Zhou, C.: Radiative forcing of the direct aerosol effect from AeroCom Phase II simulations,
1010 *Atmos. Chem. Phys.*, 13, 1853-1877, <https://doi.org/10.5194/acp-13-1853-2013>, 2013.
- 1011 Petzold, A., Rasp, K., Weinzierl, B., Esselborn, M., Hamburger, T., Dornbrack, A., Kandler, K.,
1012 Schutz, L., Knippertz, P., Fiebig, M., and Virkkula, A.: Saharan dust refractive index and optical
1013 properties from aircraft-based observations during SAMUM 2006, *Tellus B*, 61 118–130, 2009
- 1014 Petzold, A., Veira, A., Mund, S., Esselborn, M., Kiemle, C., Weinzierl, B., Hamburger, T., Ehret,
1015 G., Lieke, K., and Kandler, K.: Mixing of mineral dust with urban pollution aerosol over Dakar
1016 (Senegal): impact on dust physico-chemical and radiative properties, *Tellus B*, 63, 619-634,
1017 doi: 10.1111/j.1600-0889.2011.00547.x, 2011.
- 1018 Pistone, K., Redemann, J., Doherty, S., Zuidema, P., Burton, S., Cairns, B., Cochrane, S., Ferrare,
1019 R., Flynn, C., Freitag, S., Howell, S., Kacenelenbogen, M., LeBlanc, S., Liu, X., Schmidt, K.
1020 S., Sedlacek III, A. J., Segal-Rosenhaimer, M., Shinozuka, Y., Stamnes, S., van Diedenhoven,
1021 B., Van Harten, G., and Xu, F.: Intercomparison of biomass burning aerosol optical properties



- 1022 from in-situ and remote-sensing instruments in ORACLES-2016, *Atmos. Chem. Phys.*
1023 *Discuss.*, <https://doi.org/10.5194/acp-2019-142>, in review, 2019.
- 1024 Reid, J. S., Eck, T. F., Christopher, S. A., Koppmann, R., Dubovik, O., Eleuterio, D. P., Holben, B.
1025 N., Reid, E. A., and Zhang, J.: A review of biomass burning emissions part III: intensive optical
1026 properties of biomass burning particles, *Atmos. Chem. Phys.*, 5, 827–849, doi:10.5194/acp-5-
1027 827-2005, 2005.
- 1028 Roehrig, R., D. Bouniol, F. Guichard, F. D. Hourdin, and J. L. Redelsperger, The present and
1029 future of the west african monsoon: A process-oriented assessment of CMIP5 simulations along
1030 the AMMA transect, *J. Clim.*, 26, 6471–6505, doi:10.1175/JCLI-D-12-00505.1, 2013.
- 1031 Ryder, C. L., Highwood, E. J., Rosenberg, P. D., Trembath, J., Brooke, J. K., Bart, M., Dean, A.,
1032 Crosier, J., Dorsey, J., Brindley, H., Banks, J., Marsham, J. H., McQuaid, J. B., Sodemann, H.,
1033 and Washington, R.: Optical properties of Saharan dust aerosol and contribution from the
1034 coarse mode as measured during the Fennec 2011 aircraft campaign, *Atmos. Chem. Phys.*, 13,
1035 303–325, <https://doi.org/10.5194/acp-13-303-2013>, 2013.
- 1036 Ryder, C. L., Marengo, F., Brooke, J. K., Estelles, V., Cotton, R., Formenti, P., McQuaid, J. B.,
1037 Price, H. C., Liu, D., Ausset, P., Rosenberg, P. D., Taylor, J. W., Choularton, T., Bower, K., Coe,
1038 H., Gallagher, M., Crosier, J., Lloyd, G., Highwood, E. J., and Murray, B. J.: Coarse-mode
1039 mineral dust size distributions, composition and optical properties from AER-D aircraft
1040 measurements over the tropical eastern Atlantic, *Atmos. Chem. Phys.*, 18, 17225–17257,
1041 <https://doi.org/10.5194/acp-18-17225-2018>, 2018.
- 1042 Sakamoto, K. M., Allan, J. D., Coe, H., Taylor, J. W., Duck, T. J., and Pierce, J. R.: Aged boreal
1043 biomass-burning aerosol size distributions from BORTAS 2011, *Atmos. Chem. Phys.*, 15,
1044 1633–1646, doi:10.5194/acp-15-1633-2015, 2015.
- 1045 Sakamoto, K. M., Laing, J. R., Stevens, R. G., Jaffe, D. A., and Pierce, J. R.: The evolution of
1046 biomass-burning aerosol size distributions due to coagulation: dependence on fire and
1047 meteorological details and parameterization, *Atmos. Chem. Phys.*, 16, 7709–7724,
1048 <https://doi.org/10.5194/acp-16-7709-2016>, 2016.
- 1049 Schladitz, A., Muller, T., Kaaden, N., Massling, A., Kandler, K., Ebert, M., Weinbruch, S.,
1050 Deutscher, C., and Wiedensohler, A.: In situ measurements of optical properties at Tinfou
1051 (Morocco) during the Saharan Mineral Dust Experiment SAMUM 2006, *Tellus B*, 61, 64–78,
1052 doi:10.1111/j.1600-0889.2008.00397.x, 2009.
- 1053 Schuster, G. L., Dubovik, O., and Holben, B. N.: Angstrom exponent and bimodal aerosol size
1054 distributions, *J. Geophys. Res.*, 111, D07207, doi:10.1029/2005JD006328, 2006.



- 1055 Schwarz, J. P., et al., Coatings and their enhancement of black carbon light absorption in the
1056 tropical atmosphere, *J. Geophys. Res.*, 113, D03203, doi:10.1029/2007JD009042, 2008.
- 1057 Seinfeld, J. H. and Pandis, S. N.: Properties of the Atmospheric Aerosol, in: Atmospheric
1058 Chemistry and Physics: From Air Pollution to Climate Change, 2nd ed., John Wiley & Sons,
1059 New Jersey, USA, 350–388, 2006.
- 1060 Silva, S. and Arellano, A.: Characterizing regional-scale combustion using satellite retrievals of
1061 CO, NO₂ and CO₂, *Remote Sensing*, 9, 744, <https://doi.org/10.3390/rs9070744>, 2017.
- 1062 Solmon, F., Mallet, M., Elguindi, N., Giorgi, F., Zakey, A., and Konare, A.: Dust aerosol impact on
1063 regional precipitation over western Africa, mechanisms and sensitivity to absorption properties,
1064 *Geophys. Res. Lett.*, 35, L24705, doi:10.1029/2008GL035900, 2008
- 1065 Stier, P., Schutgens, N. A. J., Bellouin, N., Bian, H., Boucher, O., Chin, M., Ghan, S., Huneeus, N.,
1066 Kinne, S., Lin, G., Ma, X., Myhre, G., Penner, J. E., Randles, C. A., Samset, B., Schulz, M.,
1067 Takemura, T., Yu, F., Yu, H., and Zhou, C.: Host model uncertainties in aerosol radiative
1068 forcing estimates: results from the AeroCom Prescribed intercomparison study, *Atmos. Chem.*
1069 *Phys.*, 13, 3245–3270, <https://doi.org/10.5194/acp-13-3245-2013>, 2013.
- 1070 Stohl, A., Eckhardt, S., Forster, C., James, P., Spichtinger, N., and Seibert, P.: A replacement for
1071 simple back trajectory calculations in the interpretation of atmospheric trace substance
1072 measurements, *Atmos. Environ.*, 36, 4635–4648, 2002.
- 1073 Vakkari, V., Kerminen, V. M., Beukes, J. P., Tiitta, P., van Zyl, P. G., Josipovic, M., Venter, A. D.,
1074 Jaars, K., Worsnop, D. R., Kulmala, M., and Laakso, L.: Rapid changes in biomass burning
1075 aerosols by atmospheric oxidation, *Geophys. Res. Lett.*, 41, 2644–2651,
1076 doi:10.1002/2014gl059396, 2014.
- 1077 Virkkula, A., Correction of the Calibration of the 3-wavelength Particle Soot Absorption
1078 Photometer (3 λ PSAP), *Aerosol Science and Technology*, 44:8, 706–712, DOI:
1079 10.1080/02786826.2010.482110, 2010.
- 1080 Wang, T., T. F. Cheung, Y. S. Li, X. M. Yu, and D. R. Blake, Emission characteristics of CO, NO_x
1081 ,SO₂ and indications of biomass burning observed at a rural site in eastern China, *J. Geophys.*
1082 *Res.*, 107 (D12), 4157, doi:10.1029/2001JD000724, 2002.
- 1083 Weinzierl, B., Sauer, D., Esselborn, M., Petzold, A., Veira, A., Rose, M., Mund, S., Wirth, M.,
1084 Ansmann, A., Tesche, M., Gross, S., and Freudenthaler, V.: Microphysical and optical
1085 properties of dust and tropical biomass burning aerosol layers in the Cape Verde region—an
1086 overview of the airborne in situ and lidar measurements during SAMUM-2, *Tellus B*, 63, 589–
1087 618, doi: 10.1111/j.1600-0889.2011.00566.x, 2011.



- 1088 Yokelson, R. J., Crounse, J. D., DeCarlo, P. F., Karl, T., Urbanski, S., Atlas, E., Campos, T.,
1089 Shinozuka, Y., Kapustin, V., Clarke, A. D., Weinheimer, A., Knapp, D. J., Montzka, D. D.,
1090 Holloway, J., Weibring, P., Flocke, F., Zheng, W., Toohey, D., Wennberg, P. O., Wiedinmyer, C.,
1091 Mauldin, L., Fried, A., Richter, D., Walega, J., Jimenez, J. L., Adachi, K., Buseck, P. R., Hall,
1092 S. R., and Shetter, R.: Emissions from biomass burning in the Yucatan, *Atmos. Chem. Phys.*, 9,
1093 5785-5812, <https://doi.org/10.5194/acp-9-5785-2009>, 2009.
- 1094 Zhong, M. and Jang, M.: Dynamic light absorption of biomass-burning organic carbon
1095 photochemically aged under natural sunlight, *Atmos. Chem. Phys.*, 14, 1517-1525,
1096 <https://doi.org/10.5194/acp-14-1517-2014>, 2014.
- 1097 Zhai, J., Lu, X., Li, L., Zhang, Q., Zhang, C., Chen, H., Yang, X., and Chen, J.: Size-resolved
1098 chemical composition, effective density, and optical properties of biomass burning particles,
1099 *Atmos. Chem. Phys.*, 17, 7481-7493, <https://doi.org/10.5194/acp-17-7481-2017>, 2017.
- 1100 Zuidema, P., Redeman, J., Haywood, J., Wood, R., Piketh, S., Hipondoka, M. and Formenti, P.:
1101 Smoke and clouds above the southeast Atlantic: upcoming field campaigns probe absorbing
1102 aerosols impact on climate, *Bull. Am. Meteorol. Soc.*, doi: 10.1175/BAMS-D-15-00082.1,
1103 2016.
- 1104 Zuidema, P., Sedlacek III, A. J., Flynn, C., Springston, S., Delgado, R., Zhang, J., Aiken, A. C.,
1105 Koontz, A., Muradyan, P., and Zuidema, P.: The Ascension Island boundary layer in the remote
1106 southeast Atlantic is often smoky, *Geophysical Research Letters*, In Press, 4456-4465,
1107 <https://doi.org/10.1002/2017GL076926>, 2018.